

Microtubule lattice defects promote catastrophes

Ankit Rai¹, Tianyang Liu², Eugene A. Katrukha¹, Juan Estévez-Gallego³, Ian Paterson⁴,

J. Fernando Díaz³, Lukas C. Kapitein¹, Carolyn A. Moores² and Anna Akhmanova¹

¹ Cell Biology, Neurobiology and Biophysics, Department of Biology, Faculty of Science, Utrecht University, Padualaan 8, 3584 CH Utrecht, the Netherlands

² Institute of Structural and Molecular Biology, Birkbeck, University of London, Malet Street, London, United Kingdom

³ Structural and Chemical Biology, Centro de Investigaciones Biológicas Margarita Salas, Consejo Superior de Investigaciones Científicas CIB-MS, CSIC, Ramiro de Maeztu 9, 28040, Madrid, Spain

⁴ Yusuf Hamied Department of Chemistry, University of Cambridge, Cambridge CB2 1EW, United Kingdom

Corresponding author: Anna Akhmanova, a.akhmanova@uu.nl; ORCID 000-0002-9048-8614.

Abstract

Microtubules are dynamic cytoskeletal polymers that spontaneously switch between phases of growth and shrinkage. The probability of transitioning from growth to shrinkage, termed catastrophe, increases with microtubule age, but the underlying mechanisms are poorly understood. Here, we set out to test whether microtubule lattice defects formed during polymerization can affect growth at the plus end. To generate microtubules with lattice defects, we used microtubule-stabilizing agents that promote formation of polymers with different protofilament numbers. By employing different agents during nucleation of stable microtubule seeds and subsequent polymerization phase, we could reproducibly induce switches in protofilament number. Such switches led to frequent catastrophes, which were not observed when microtubules were grown in the same conditions but without a protofilament number mismatch. Microtubule severing at the site of the defect was sufficient to suppress catastrophes. We conclude that structural defects within microtubule lattice can affect the dynamic state of the plus end.

Introduction

Microtubules are cytoskeletal polymers that rapidly switch between phases of growth and shortening, and this behavior, termed dynamic instability, plays a crucial role in the formation, maintenance and reorganization of microtubule arrays during cell division, migration and differentiation^{1, 2}. The transition from growth to shrinkage, an event called catastrophe, is known to occur when the protective cap of GTP-bound tubulin subunits is reduced or lost, but the underlying mechanisms are still subject of investigation^{3, 4}. One interesting property of microtubules is that the frequency of catastrophes depends on microtubule age: microtubules that are growing for a longer time have a higher chance to switch to depolymerization^{5, 6}. Changes occurring at the microtubule end, such as loss of individual rows of tubulin subunits (termed protofilaments) or end tapering have been shown to promote catastrophe⁷⁻⁹. In principle, it is also possible that the catastrophe frequency at the plus end is affected by structural features in the microtubule lattice further away from the tip, but this possibility has so far remained untested.

Structural studies have established that tubulin can form tubes with different protofilament numbers, dependent on the species, nucleation template, presence of different microtubule-associated proteins and other properties of the polymerization reaction (e.g.¹⁰, reviewed in¹¹). An important consequence of the structural plasticity of the microtubule lattice¹² is the formation of lattice defects, such as sites where a microtubule gains or loses one or more protofilaments^{10, 13-16}. Such sites can be introduced during microtubule growth, and their presence may affect microtubule dynamics in different ways. For example, defects can be repaired through tubulin incorporation, and the resulting islands of GTP-tubulin can trigger microtubule rescue¹⁷⁻²⁰. On the other hand, the presence of defects could potentially also induce catastrophes (as proposed in ref¹³), since conformational properties of the microtubule lattice might propagate over some distances²¹.

To study the relationship between lattice defects and microtubule catastrophes, one should be able to detect defects in real time and correlate their presence with the dynamics of microtubule ends. Our recent insights obtained from microtubules grown in the presence of low doses of microtubule-stabilizing agents (MSAs), such as Taxol, its fluorescent analog Fchitax-3 or Epothilone B, suggested a way to perform such experiments. We found that MSAs preferentially bind to microtubule plus ends entering a "pre-catastrophe" state²². This state is manifested by the gradual loss of the GTP cap and can be detected by reduced recruitment of End Binding (EB) proteins, which detect GTP-bound microtubule lattice²³⁻²⁶. Increased MSA accumulation at a microtubule end prevented microtubule depolymerization and led to the formation of a stabilized patch of microtubule lattice, where the tube was incomplete and continuously incorporated GTP-tubulin but was not fully repaired²². Such persistent lattice defects (termed "stable rescue sites") could induce repeated rescues when microtubules switched to depolymerization²².

Here, we used MSA-induced lattice defects to address two questions. First, what prevents complete repair of the microtubule discontinuity at the stable rescue site? And second, does the presence of a lattice defect affect the dynamic properties of the microtubule plus end, such as the rate of catastrophe induction? Since the presence of different MSAs is known to affect the number of protofilaments^{14, 27-33}, we hypothesized that persistent lattice defects observed in our experiments could be associated with changes in protofilament number and thus could not be fully repaired for geometrical reasons. We tested this idea by generating stable microtubule seeds with one MSA and then elongating them in the presence of another MSA, which had preference for a microtubule lattice with the same or different number of protofilaments. Use of fluorescent MSAs allowed us to directly follow drug binding. In agreement with our previous study²², we found that the pre-catastrophe state of the microtubule plus end triggered drug binding in all

conditions; however, the outcome of drug binding was different. Large and persistent drug accumulations were only formed when, based on the MSA properties, a mismatch in protofilament number could be expected; the existence of such mismatches was confirmed by cryo-electron microscopy (cryo-EM) and by measuring microtubule growth rate, which varied dependent on protofilament number. Interestingly, when microtubule ends extended beyond a mismatch-containing lattice defect, they displayed elevated catastrophe frequency. In contrast, in conditions when the microtubule seed and the elongating microtubule had the same protofilament number, drug accumulations were short in duration and length, and microtubule growth beyond such sites was much more processive. Laser-mediated severing of a microtubule at the site of lattice defect in conditions of protofilament mismatch could reduce catastrophe frequency at the plus end. These data demonstrate that local properties of the microtubule lattice, such as defects, can affect the state of the dynamic end tens of micrometers away.

Results

Protofilament number affects microtubule growth rate

Protofilament number in microtubules changes in response to the nucleotide bound to the regulatory E-site or the presence of MSAs^{14, 27-33}. To generate microtubules with different protofilament numbers, we prepared microtubule seeds with the slowly hydrolysable GTP analog GMPCPP or with different microtubule-stabilizing drugs. Using X-ray fiber diffraction and cryo-EM, we confirmed previous observations showing that microtubule seeds generated in the presence of Taxol have predominantly 12/13 protofilaments (pf), whereas 14pf microtubules were observed in the presence of GMPCPP and Docetaxel (Fig. 1a,b)^{14, 30-33}. Microtubules stabilized with Alexa₄₈₈-Epothilone B also had 14pf, whereas protofilament number shifted

towards 15pf in the presence of Discodermolide and 15/16pf with Fchitax-3 (Fig. 1a,b). We next used these different stabilized microtubule seeds to grow dynamic microtubules and observed their behavior using Total Internal Reflection Fluorescence Microscopy (TIRFM) as described previously^{34, 35} (Supplementary Fig. 1a). Assays were performed either with tubulin alone or with the addition of mCherry-EB3, which serves as microtubule plus end marker and increases both the growth rate and catastrophe frequency in assays with purified tubulin³⁶ (Fig. 1c, Supplementary Fig. 1b). In these assays, MSAs were used to prepare stable seeds but were not added during polymerization. Both with and without EB3, we found that microtubule growth rate increased with the protofilament number, while catastrophe frequency showed some variability between different conditions but was independent of protofilament number (Fig. 1d,e, Supplementary Fig. 1c,d). As described previously³⁵, very few rescues were seen when microtubules were grown from GMPCPP seeds, while occasional rescues were found when drug-stabilized seeds were used, likely because some drug molecules could diffuse from the seeds and bind to the dynamic lattice. Importantly, in these conditions, drugs present in the seeds had no effect on the polymerization rate - for example, all microtubules grown from 14pf seeds, including GMPCPP-stabilized ones, polymerized with the same speed. We confirmed these results by labeling seeds with different protofilament numbers in different colors and growing microtubules from two types of seeds on the same coverslip: for example, in the same reaction mix, microtubules grew from Taxol-stabilized seeds slower than from GMPCPP seeds (Supplementary Fig. 2a). We also investigated whether microtubule depolymerization rate depended on protofilament number but found no clear correlation: we observed that microtubules grown from 14pf or 15/16pf seeds depolymerized at the same rate, but slower than microtubules grown from Taxol-stabilized (12/13pf) seeds (Supplementary Fig. 2b). We conclude that when

the growth conditions are the same, microtubule polymerization but not depolymerization rate can be used to infer protofilament number.

Effects of MSAs on microtubule dynamics depend on the protofilament number in the seeds

Next, we modified the assay by adding MSAs during polymerization (Fig. 2a). Drug concentrations in the range 50-400 nM were used, because higher concentrations induced spontaneous microtubule nucleation, and we thus could not ensure that all observed microtubules grew from the pre-existing seeds with the known protofilament number. We observed three types of dynamic microtubule behaviors: semi-processive growth interrupted by short (<0.5 μm) depolymerization events followed by rapid rescues (Type 1, Fig. 2b,c); frequent catastrophes followed by long (>0.5 μm) depolymerization events and repeated rescues at the same site (“stable rescue site”, Type 2, Fig. 2b,c) and catastrophes followed by long depolymerization events and randomly distributed rescues (Type 3, Fig. 2b,d). At 100 nM MSA concentrations, there was a clear difference in the occurrence of a particular type of dynamics, which depended on the combination of MSAs used for preparing the seeds and their elongation. When the protofilament number was expected to be the same (“matching conditions”, Fig. 2a), Type 1 dynamics with very short depolymerization events strongly predominated (Fig. 2b,c, Supplementary Fig. 3a,b). In contrast, when the seeds were elongated in the presence of an MSA that had a protofilament number preference that was different from that of the MSA used for seed stabilization (“mismatching conditions”, Fig. 2a), Type 2 or Type 3 dynamics with frequent catastrophes and long depolymerization events were observed (Fig. 2b-d, Supplementary Fig. 3a,b). When higher MSA concentrations were used during microtubule growth, Type 3 dynamics was predominantly observed for mismatching conditions (Fig. 2e), likely because rescues became more frequent, and depolymerization events were thus not long enough to reach the preceding

stable rescue site. When MSA concentration was reduced, we also observed some microtubules displaying Type 3 dynamics in matching conditions, because depolymerization events became somewhat longer but were typically still followed by rapid rescues (Fig. 2f).

Importantly, microtubules grown in the presence of the same MSA showed very different dynamics dependent on the seeds used. For example, microtubules grown in the presence of 100 nM Taxol displayed Type 1 dynamics when grown from Taxol-stabilized seeds (13pf), but Type 2 or Type 3 dynamics when grown from GMPCPP-stabilized (14pf) or Fchitax-3 stabilized (15/16pf) seeds (Fig. 2b,c, Supplementary Fig. 3a,b). In contrast, in the presence of Docetaxel, microtubules grew with Type 1 dynamics from GMPCPP or Docetaxel-stabilized (14 pf) seeds but showed Type 2/3 dynamics when grown from Taxol- or Fchitax-3 stabilized seeds (Fig. 2b,c, Supplementary Fig. 3a,b). Similar results were also observed when microtubules were grown without mCherry-EB3, although the absence of a plus-end marker made the detection of short depolymerization events less reliable (Supplementary Fig. 4). For subsequent analyses, we therefore focused on the data obtained with MSA concentrations of 100 nM in the presence of mCherry-EB3. Together, these results demonstrate that the (mis)match between the protofilament number of the seed and the number preferred by the MSA present during elongation has a strong effect on microtubule growth dynamics, even when the microtubule tip is far away from the seed.

Larger and more persistent drug accumulations are observed in mismatching conditions

To better understand the origin of the observed differences in microtubule dynamics, we analyzed in detail the binding of fluorescent drugs in different conditions. In our previous study, we showed that stable rescue sites (Type 2 dynamics) appear due to the formation of extended drug accumulations²². These accumulations initiate directly behind a growing microtubule plus end entering a pre-catastrophe state, which can be distinguished by the reduction in EB3 signal²².

Indeed, in mismatching conditions, such as GMPCPP seeds (14pf) elongated in the presence of Fchitax-3 (15/16pf) (our previous study²²) or Taxol-stabilized seeds (13pf) elongated in the presence of Alexa₄₈₈-Epothilone B (14pf), we observed large and persistent drug accumulations that led to formation of stable rescue sites (Fig. 3a,b). In contrast, in matching conditions (GMPCPP-stabilized seeds elongated in presence of Alexa₄₈₈-Epothilone B (14pf) or Fchitax-3-stabilized seeds elongated in the presence of Fchitax-3 (15/16pf), only drug accumulations that were short in duration and length were observed (Fig. 3c-e, Supplementary Fig. 5a). Similar to stable rescue sites, these regions of increased drug binding were always initiated directly behind a microtubule plus end that underwent a growth perturbation, which could be detected by the gradual reduction of the mCherry-EB3 signal. We obtained curves of mCherry-EB3 and Fchitax-3 intensities during drug accumulation events and aligned them along the time axis by maximizing cross-correlation between Fchitax-3 time curves (Fig. 3f). The initial phase of drug accumulation was very similar for matching conditions (growth in the presence of Fchitax-3 from Fchitax-3-stabilized seeds) and mismatching conditions (growth in the presence of Fchitax-3 from GMPCPP-stabilized seeds) (Fig. 3f). The kinetics of reduction of EB3 signal before drug binding showed considerable variability but displayed no striking differences for both conditions (Fig. 3f).

Importantly, growth perturbations in matching conditions were typically of limited duration and were often accompanied by the emergence of a second, faster comet at the rear of the drug accumulation site (Fig. 3c,d, Supplementary Fig. 5a). Our previous studies showed that such a “catching up” comet appears when some protofilaments at the growing microtubule tip are stalled whereas the others keep elongating. When the stalled protofilaments start to regrow, this is manifested by the appearance a faster rear comet that ultimately fuses with the leading one^{8, 37}. Such split comets were previously readily observed in the presence of the microtubule-stabilizing

protein CLASP, which, similar to Fchitax-3, appears to have a preference for the microtubule region behind the growing microtubule tip³⁷. The appearance of split comets during growth perturbations was observed in all the tested matching conditions, also when non-fluorescent MSAs were used (Supplementary Fig. 5b,c). Clear split comets were seen in 38-79% of all catastrophe (growth perturbation) events detected in matching conditions (Fig. 3g). Since the two comets must be located at a significant distance from each other to be registered as a “split comet” by fluorescence microscopy, these numbers likely provide underestimates of the actual frequency of such events, suggesting that formation of a “catching up” comet is a major mechanism preventing long depolymerization episodes after growth perturbations in matching conditions.

Taken together, the data suggest that in both matching and mismatching conditions, enhanced MSA binding occurs directly behind pre-catastrophe microtubule tips and this binding prevents the actual catastrophe. The binding density of Fchitax-3 in matching conditions (0.3-0.9 molecules per 8 nm microtubule length, Supplementary Fig. 5d) was somewhat lower than that found in large Fchitax-3 accumulations in mismatching conditions (~1-2 drug molecules per 8 nm (ref ²²)). This can be explained by the fact that in matching conditions, drug-bound pre-catastrophe microtubule ends appear to be restored rapidly, likely because lagging protofilaments regrow forming a “catching up” comet, and this would lead to tube closure and prevent further drug accumulation. In contrast, in mismatching conditions, drug accumulations expand for a longer time, possibly because a normal tube is more difficult to restore and protofilaments continue growing as a sheet or some other microtubule end structure that promotes drug binding. Ultimately, also in mismatching conditions the drug accumulation abruptly ceases (Fig. 3a,b), possibly due to tube closure. Thus, a mismatch between the protofilament number preference of

the MSA used to prepare the seeds and to elongate them inhibits the restoration of a growing microtubule plus end after a drug accumulation has formed.

Lattice defects observed in mismatching conditions are associated with switching of protofilament number

We hypothesized that binding of the drug to a pre-catastrophe microtubule tip either induces or stabilizes tubes with a protofilament number fitting with the specific preference of the drug used. In mismatching conditions, this would cause a protofilament number switch occurring at the stable rescue site, and this could explain why such sites do not get fully repaired. If this hypothesis is correct, a microtubule will be expected to grow with the speed characteristic for the number of protofilaments present in the seed before the stable rescue site, but with a speed characteristic for the MSA present in the growth reaction after it. We found that in matching conditions, the addition of any MSA caused an increase in microtubule growth rate, but the correlation between the rate and protofilament number was retained (Fig. 4a). Interestingly, microtubules with Type 2 dynamics in mismatching conditions displayed growth rates characteristic for the seed before the rescue site and the growth rate matching better that of the MSA used in the growth reaction after the stable rescue site. For example, when GMPCPP seeds (14pf) were elongated in the presence of Fchitax-3 (15/16pf) or Taxol (13pf), the growth rate was characteristic for 14pf microtubules before the stable rescue site but was elevated after it in the presence of Fchitax-3 and decreased in the presence of Taxol (Fig. 4a). In contrast, in matching conditions, growth rate before and after a growth perturbation did not change (Supplementary Fig. 6a). It should be noted, however, that the changes in growth rate did not completely match the speeds of microtubule growth when the same MSA was used for seed stabilization and

elongation (Fig. 4a). This likely reflects variability in protofilament number after the switch at a stable rescue site.

Further support for the occurrence of protofilament number switching at the stable rescue sites was obtained by cryo-EM. In our previous study²², we found that microtubule lattice discontinuities corresponding to Fchitax-3 accumulations can be detected by cryo-EM. Here, we re-analyzed these data focusing on the microtubule diameter at the two sides of a lattice defect and found that protofilament number changed in ~53% of such cases, whereas in microtubules lacking defects switches in protofilament number were rare (Fig. 4b, Supplementary Fig. 6b). Thus, MSAs present during microtubule elongation can induce a switch to their preferred protofilament number at the stable rescue site.

Protofilament number mismatch between the seed and the growing microtubule lattice promotes catastrophes

Having established that stable rescue sites can correspond to regions where a switch in protofilament number takes place, we next asked how such sites affect growth of microtubules extending beyond them. Interestingly, we found that whereas catastrophe frequency (calculated as frequency of all growth perturbations including “catching up” events) remained constant for microtubules growing in matching conditions, it was strongly increased for the growth events occurring after the stable rescue site (Fig. 4c). The increase in catastrophe frequency was similar for microtubules that switched to higher (e.g. from 13pf or 14pf to 15/16pf) or lower (from 14pf to 13pf) number of protofilaments (Fig. 4c). This observation was surprising, because one would expect that after switching to the protofilament number “preferred” by the MSA present in solution, a microtubule will be further growing in matching conditions and should thus display Type 1 dynamics (short growth perturbations followed by quick repair) instead of Type 2/3

dynamics with long depolymerization events. Strikingly, we found that this was not the case, because microtubule plus ends entering a pre-catastrophe state after a stable rescue site typically did not accumulate MSAs and were not repaired by “catching up” events but instead switched to depolymerization, which typically proceeded all the way back to the preceding stable rescue site (Fig. 3a,b). MSA accumulations at the pre-catastrophe tips after a stable rescue site (Fig. 4d) were rare: for example, formation of a secondary stable rescue site on microtubules extended from GMPCPP-stabilized seeds in the presence of Fchitax-3 happened only in 11% of all observed microtubules, with no difference in the growth rate before and after the formation of second stable rescue site (Fig. 4d). Whereas 48% of all catastrophe events occurring during microtubule outgrowth from the seed led to drug accumulation and formation of a stable rescue site, only 5% of catastrophes occurring after a stable rescue site triggered drug accumulation and microtubule stabilization (Fig. 4e, left panel). Further, when we considered only the microtubules which showed formation of two consecutive stable rescue sites, only 19% of catastrophes occurring after a stable rescue site triggered drug accumulation compared to 72% of catastrophe events occurring during initial outgrowth from the seed, before the first stable rescue site was formed (Fig. 4e, right panel). This suggests that some properties of a pre-catastrophe microtubule plus end extending after a stable rescue site (after a microtubule has incorporated a lattice defect) are different from those of microtubule ends growing directly from the seed.

To explore the underlying mechanism, we analyzed the intensities of EB3 comets and microtubule tip tapering during growth episodes from the GMPCPP-stabilized seed (14pf) either in the absence of drugs (control) or after a stable rescue site induced by Discodermolide (14/15pf, mismatching conditions). We note that Fchitax-3 or Alexa₄₈₈-Epothilone B could not be used in these experiments because we used green (HiLyte 488TM labeled tubulin) fluorescence to obtain tubulin profiles. We focused on the 40 s time interval preceding a catastrophe in order to

determine whether the pre-catastrophe plus ends of microtubules growing directly from the seed or from a stable rescue site are somehow different. Microtubule end tapering was similar, though in the last 10s before catastrophe there was a very mild trend for increased tapering in microtubule plus ends growing from seeds compared to the plus ends growing after a Discodermolide-induced stable rescue sites (Fig. 4f). The reduction of EB3 signal during catastrophe onset, which is expected to reflect the kinetics of GTP cap loss during catastrophe initiation, did show a subtle difference – the curve was somewhat less steep for microtubules growing from seeds compared to microtubules elongating beyond a stable rescue site (Fig. 4g). Since drug binding occurs after the EB3 signal is partially reduced (Fig. 3f), it is possible that a more gradual change in the plus end structure provides a window of opportunity for the drug to bind, explaining why pre-catastrophe plus ends are more frequently stabilized by drug accumulation when they grow from the seed than after a stable rescue site.

Microtubule severing at the lattice defect site suppresses catastrophes

Why do microtubules growing beyond a stable rescue site display more catastrophes and have a steeper EB3 decay pattern? One possibility is that a lattice defect with a different number of protofilaments on the two sides affects the growth at the plus end through a long-range conformational alteration or a mechanical signal. If this is the case, severing the microtubule at the site of the defect should reduce catastrophe frequency (Fig. 5a). We note that after microtubule severing in the absence of MSAs (microtubules polymerized in the presence of GMPCPP seeds with 15 μ M tubulin and 20 nM EB3), freshly generated microtubule plus ends typically depolymerized, whereas freshly generated minus ends displayed heterogeneous behavior. ~50% of newly generated microtubule minus ends depolymerized rapidly after severing and ~20% of the minus end depolymerized slowly, while the remaining ~30% of microtubules

had stable minus ends and eventually depolymerized from the plus end. The poor survival of microtubules after severing and the heterogeneity in minus-end dynamics precluded a meaningful analysis of the severing data for control microtubules in the absence of MSAs.

In the presence of an MSA such as Fchitax-3, both severed ends were typically stabilized (Fig. 5b). Interestingly, when we severed microtubules at the site of Fchitax-3 accumulation (a stable rescue site), the catastrophe frequency at the plus end of the newly generated microtubule fragment distal from the seed (with the minus end located at the former stable rescue site) significantly decreased and a large proportion of microtubules switched from Type 2 dynamics (long depolymerization episodes) to Type 1 dynamics (semi-processive growth with short depolymerization episodes) (Fig. 5b,c,e). In contrast, microtubules remained catastrophe-prone and exhibited Type 2 dynamics if we severed microtubules at a location preceding a stable rescue site (Fig. 5c-e). These data support the idea that lattice discontinuities can have long-range effects on microtubule plus end dynamics.

Discussion

In this study, we addressed how microtubule lattice defects affect growth at the microtubule plus end. We made use of our previous data showing that when microtubules are grown in the presence of non-saturating concentrations of MSAs, such as taxanes, the drugs strongly bind to microtubule ends in a pre-catastrophe state and thereby induce regions of increased microtubule stability, termed stable rescue sites²². Importantly, these sites can contain “holes” in the microtubule wall, where fresh tubulin can be incorporated²². In the current study, we show that these sites represent areas of alterations in protofilament number, providing a simple geometrical reason for the persistence of defects over time, despite continuous microtubule repair. This interpretation is supported both by cryo-EM data and by measuring microtubule growth speeds,

which we found to correlate with protofilament number. It is important to note that the exact structural nature of these defects is likely to be complex. For example, recent cryo-EM work has shown that microtubules are not perfectly cylindrical but display strong local deviations from helical symmetry with different lateral contact geometries, and these deviations can be affected by taxanes³⁸. Local deviations from a cylindrical shape and additional types of microtubule lattice conformations, such as microtubule sheets, will likely have a major impact on the defect structure, stability and affinity for MSAs. Understanding the heterogeneity of lateral contacts between tubulin dimers, including the occurrence of “seam-like” contacts between α - and β -tubulin that varies dependent on protofilament number, might also help to explain the dependence of microtubule growth rate on protofilament number.

Reproducible generation of lattice defects by using different MSAs allowed us to explore the consequences they have on microtubule dynamics (Fig. 5f). Strikingly, we found that although a microtubule could polymerize beyond a persistent lattice defect for lengths up to several micrometers, microtubule plus end dynamics were affected, as the catastrophe frequency after the defect was significantly increased (Fig. 5f). We observed that the decay in EB3 intensity before a catastrophe occurred somewhat more gradually after a seed than after a stable rescue site. We also cannot exclude that the microtubule plus ends were slightly less tapered after a stable rescue site, but the resolution of our fluorescence microscopy-based assay was insufficient to investigate whether this difference was significant. The most notable difference between microtubule plus ends grown from defect-bearing stable rescue sites and from stabilized seeds was that the latter could be efficiently “rescued” by an MSA once they entered a pre-catastrophe state. Drug accumulations leading to microtubule stabilization were ~10 more frequent at the pre-catastrophe tips growing from seeds compared to microtubule ends entering a catastrophe after a preceding stable rescue site. These data indicate that some conformational aspects of a pre-

catastrophe plus end during growth after a seed are different from those of a plus end elongating beyond a stable rescue site, and this might reflect differences in the catastrophe induction mechanism.

Strikingly, when microtubules were growing in matching conditions (when the MSAs used to stabilize the seeds and to elongate them had the same protofilament number preference), almost every growth perturbation resulted in rapid drug binding and tip repair, leading to semi-processive microtubule growth. These data show that the state and dynamics of the microtubule plus end depend not just on the conditions of polymerization, but also on the state of the preceding lattice (Fig. 5f). For example, microtubules growing in the presence of 100 nM Fchitax-3 from an Fchitax-3-stabilized seed and from a GMPCPP-stabilized seed after a stable rescue site encounter exactly the same concentrations of the drug and tubulin. Yet, in the first case, microtubule polymerization is somewhat faster and semi-processive, because although growth perturbations still occur just as in the absence of MSAs, microtubule ends transitioning to catastrophe are quickly repaired through “catching up” events. In contrast, microtubules plus ends growing in the same conditions from a stable rescue site (i.e. after a lattice defect) undergo frequent catastrophes and are not repaired through MSA binding. Therefore, in mismatching conditions, catastrophes typically evolve into long depolymerization episodes.

Importantly, microtubule severing at the site of the defect made microtubules less catastrophe-prone, in line with the view that a lattice defect at the stable rescue site has propagating properties. The underlying mechanism is unclear, but it is possible that both tubulin extension or compaction in the axial direction^{39, 40} and changes in angles between protofilaments due to heterogeneity of lateral contacts³⁸ might play a role. One surprising feature of the drug effects in our experiments is that they can be exerted at quite low drug binding densities (in some cases, less than 1 drug molecule per 8 nm of microtubule length or one tubulin “ring”). This

suggests that effects of drug binding to a single tubulin dimer can propagate within the microtubule lattice. This is comparable to the reported effect of kinesin-1, where a few molecules binding to a microtubule could affect the structural properties of this microtubule⁴¹.

The finding that lattice defects have a propagating impact on microtubule plus end dynamics has important consequences for the concept of microtubule ageing. Previous work showed that the catastrophe frequency increases when a microtubule grows for a longer time, indicating that multiple steps are needed to induce a catastrophe^{5, 6}. However, the nature of these steps is still unclear: they may be associated with a gradual change in the microtubule end structure (e.g. more tapering)^{7, 9, 42}, but may also occur within the lattice. Both types of changes might play a role, and in fact, our data suggest that the mechanistic basis of catastrophe induction may differ, as pre-catastrophe microtubule tips can be different both in terms of drug accumulation and EB3 decay. We found that the occurrence of lattice defects associated with protofilament number mismatch leads to catastrophe, and since such defects can accumulate over time, they can potentially contribute to microtubule aging. Lattice defects including switches in protofilament number have been extensively documented in previous studies^{10, 13-16}. The associated microtubule repair has been described both *in vitro* and in cells, but until now, microtubule lattice discontinuities have been mostly associated with formation of GTP islands, rescues and microtubule stabilization^{17-20, 43}. Here, we show that catastrophe induction is another important consequence of defects associated with loss or acquisition of protofilaments. Our results suggest that switches in protofilament number would have a destabilizing effect on microtubules, a possibility that would need to be explored in cells.

Methods

Reagents and purified proteins

Taxol, 1,4-piperazinediethanesulfonic acid (PIPES), GTP, methylcellulose, glucose oxidase from *Aspergillus niger*, catalase from bovine liver, dithiothreitol (DTT), magnesium chloride, ethylene glycol-bis(2-aminoethylether)-N,N,N',N'-tetraacetic acid (EGTA), potassium chloride, potassium hydroxide, κ -casein and glucose were obtained from Sigma-Aldrich. GMPCPP was obtained from Jena Biosciences. Biotinylated poly(l-lysine)-[g]-poly(ethylene glycol) (PLL-PEG-biotin) was obtained from Susos AG. NeutrAvidin was obtained from Invitrogen. Different types of labelled and unlabeled purified tubulin used in the assays were either purchased from Cytoskeleton or purified as described previously⁴⁴ for X-ray fiber diffraction experiments.

Docetaxel was procured from Sanofi-Aventis. Fchitax-3 was provided by Wei-Shuo Fang (State Key Laboratory of Bioactive Substances and Functions of Natural Medicines, Institute of Materia Medica, Beijing, China⁴⁵). Alexa₄₈₈-Epothilone B was obtained from Simon Glauser and Karl-Heinz Altman (Department of Chemistry and Applied Biosciences, Institute of Pharmaceutical Sciences, ETH Zürich, Zurich, Switzerland²²). Discodermolide was synthesized as described previously⁴⁶.

X-ray fiber diffraction

X-ray fiber diffraction images were collected in beamline BL11-NCD-SWEET of ALBA Synchrotron. Purified bovine tubulin (5 mg) was diluted to a final concentration of 100 μ M in PM buffer (80 mM PIPES, 1 mM EGTA, 0.2 mM Tris, 1 mM DTT), containing 3 mM MgCl₂, 2 mM GTP and 200 μ M of the corresponding compound. Samples were incubated at 37 °C for 30 min to achieve maximum polymerization and then were mixed in a 1:1 volume ratio with pre-warmed PM buffer containing 3 mM MgCl₂ and 2% Methylcellulose (MO512, Sigma-Aldrich).

Final concentrations of protein, nucleotide and compounds were 50 μ M tubulin, 1 mM GTP and 100 μ M of compound. Samples were centrifuged for 10 s at 2000 g to eliminate air bubbles and transferred to a share-flow device^{47, 48}.

For each condition, 24 diffraction images were averaged and background subtracted using ImageJ software (version 1.51j8; Wayne Rasband, National Institutes of Health, Bethesda, USA). Angular image integrations were performed using XRTools software (obtained upon request from beamline BM26-DUBBLE of the European Synchrotron Radiation Facility (ESRF)). For average protofilament number determination, image analysis was performed as previously described⁴⁹ considering the absolute position of J01 for Taxol (0.0518 nm) as the reference for determining the relative peak positions for the remaining assayed conditions.

Cryo-Electron Microscopy

Microtubule polymerization: For the analysis of protofilament number distribution, microtubules in the presence of GMPCPP or drugs were polymerized as described below in the section on microtubule dynamics, but in the absence of rhodamine- or biotin-labeled tubulin. For protofilament number transition analysis, microtubules were polymerized from GMPCPP seeds with 1 mM GTP, 15 μ M tubulin, 20 nM mCherry-EB3 in the presence of 100 nM Fchitax-3 at 37 °C for 10 min.

Sample preparation: 4 μ l of each microtubule sample was applied to holey carbon grids (C-flat 2/2, Protochips) glow-discharged in air, before blotting and plunge-freezing using a Vitrobot Mark IV (Thermo Fisher Scientific) at 22 °C and 100% humidity.

Cryo-EM data collection: For protofilament number distribution analysis, cryo-EM micrographs of Taxol and GMPCPP MTs were collected on a Tecnai T12 transmission electron microscope (Thermo Fisher Scientific) with a 4x4K CCD camera (Gatan), operating at 120 kV, image pixel

size of 2.09 Å and defocus of around -5 µm. Cryo-EM micrographs of Fchitax-3 MTs were collected on a G2 Polara transmission electron microscope (Thermo Fisher Scientific) with a K2 Summit detector, operating in counting mode and with a GIF Quantum LS Imaging Filter (Gatan) at 300kV, image pixel size of 1.39 Å and defocus range from -1.5 to -4 µm. 40 frames were motion corrected using MotionCor2⁵⁰. For protofilament number transition analysis, cryo-EM images of MTs were collected on a Tecnai T12 (Thermo Fisher Scientific) as above.

Cryo-EM data analysis: For protofilament number distribution analysis, protofilament number was determined by Moiré pattern visualization. 50-90 microtubules were selected for each dataset. For each microtubule population, the percentage of microtubules with a particular protofilament number was calculated.

For protofilament number transition analysis, microtubule diameters on each side of sheet-like lattice defects in Fchitax-3-microtubules were measured manually in Fiji. Diameters of equivalently separated sides of intact MTs were measured as controls. To aid diameter measurement, Fourier transforms of microtubule regions were computed and filtered to enhance microtubule Moiré patterns. The filtered Fourier transforms were then inverse transformed to give filtered microtubule images.

In vitro assay for microtubule dynamics

In vitro assay for microtubule growth dynamics was performed as described previously^{34, 35}. Briefly, as described earlier²², microtubule seeds stabilized in the presence of GMPCPP (a slowly hydrolyzable GTP analog) were prepared by two rounds of polymerization and depolymerization in the presence of GMPCPP. A solution of 20 µM porcine brain tubulin mix containing 12% rhodamine-labeled tubulin/HiLyte 488TM labeled tubulin and 18% biotin-labeled tubulin was

polymerized in MRB80 buffer (80 mM K-PIPES, pH 6.8, 1 mM EGTA, 4 mM MgCl₂) in the presence of GMPCPP (1 mM) at 37 °C for 30 min. After polymerization, the mixture was pelleted by centrifugation at 119,000 × g for 5 min in an Airfuge centrifuge. Obtained pellet was resuspended in MRB80 buffer and microtubules were depolymerized on ice for 20 min. The resuspended mixture was further polymerized in the presence of GMPCPP. After the second round of polymerization and pelleting, GMPCPP-stabilized microtubule seeds were stored in MRB80 containing 10% glycerol. For preparing microtubule seeds in the presence of microtubule stabilizing agents (MSAs), a solution of porcine brain tubulin (40 μM) mix containing biotin-labeled tubulin (18%) and rhodamine-labeled tubulin (12%) was polymerized in MRB80 buffer (80 mM K-PIPES, pH 6.8, 4 mM MgCl₂, 1 mM EGTA) in the presence of GTP (1 mM) and indicated MSAs (20 μM) at 37 °C for 20 min. 20 μM MSAs (Taxol, Docetaxel, Alexa488-Epothilone B, Discodermolide and Fchitax-3) diluted in MRB80 were prewarmed to 37°C. Polymerizing tubulin solution was diluted 5 times with prewarmed 20 μM MSA solution and incubated further for 5 mins. The solution was centrifuged at 13200 × g for 15 min at 30 °C. Obtained pellet was resuspended in 20 μM MSA solution (diluted in MRB80) and stored at room temperature with protection from light.

In vitro flow chambers were assembled on microscopic slides with plasma-cleaned glass coverslips using two strips of double-sided tape. Flow chambers were sequentially incubated with PLL-PEG-biotin (0.2 mg/ml) and NeutrAvidin (1 mg/ml) in MRB80 buffer. The chamber was further incubated with GMPCPP stabilized microtubule seeds followed by treatment with 1 mg/ml κ-casein in MRB80 buffer. The reaction mixtures containing 15 μM porcine brain tubulin supplemented with 3% rhodamine-tubulin when indicated, 20 nM mCherry-EB3 when indicated, 50 mM KCl, 0.1% methylcellulose, 0.2 mg/ml κ-casein, 1 mM guanosine triphosphate and oxygen scavenger mixture (50 mM glucose, 400 μg/ml glucose oxidase, 200 μg/ml catalase, and

4 mM DTT in MRB80 buffer) with or without MSAs were added to the flow chambers after centrifugation in an Airfuge for 5 minutes at $119,000 \times g$. The chambers were sealed with vacuum grease, and microtubule dynamics was recorded using TIRF microscopy. All samples were imaged at 30 °C.

Image acquisition by TIRF microscopy

Imaging was performed on a TIRF microscope setup (inverted research microscope Nikon Eclipse Ti-E) which was equipped with the perfect focus system (PFS) (Nikon) and Nikon CFI Apo TIRF 100x 1.49 N.A. oil objective (Nikon, Tokyo, Japan). The microscope was supplemented with TIRF-E motorized TIRF illuminator modified by Roper Scientific France/PICT-IBiSA Institut Curie, and a stage top incubator model INUBG2E-ZILCS (Tokai Hit) was used to regulate the temperature of the sample. Image acquisition was performed using either a Photometrics Evolve 512 EMCCD camera (Roper Scientific, final magnification 0.063 $\mu\text{m}/\text{pixel}$) or a Photometrics CoolSNAP HQ2 CCD camera (Roper Scientific, final magnification 0.063 $\mu\text{m}/\text{pixel}$) or a Prime BSI sCMOS camera (Teledyne Photometrics, final magnification 0.068 $\mu\text{m}/\text{pixel}$) and controlled with MetaMorph 7.7 software (Molecular Devices, CA). For simultaneous imaging of red and green fluorescence, we used a triple-band TIRF polychroic ZT405/488/561rpc (Chroma) and a triple-band laser emission filter ZET405/488/561m (Chroma), mounted in a metal cube (Chroma, 91032) together with an Optosplit III beamsplitter (Cairn Research Ltd, Faversham, UK) equipped with double emission filter cube configured with ET525/50m, ET630/75m and T585LPXR (Chroma). Images were captured with 5 frames/s in stream acquisition mode for Supplementary Fig. 2b and Fig. 5b, 1 frame/s in time lapse mode for Fig. 3f and 1 frame/2s in time lapse mode for rest of the data.

Analysis of microtubule dynamics in vitro

For Image analysis, ImageJ plugin KymoResliceWide v.0.4 (<https://github.com/ekatruxha/KymoResliceWide> (Katrukha, 2015)) was used for generating kymographs to represent the life history of microtubule dynamics. Microtubule dynamics parameters using kymographs were measured manually. The length and the duration of each growth event were measured as horizontal and vertical distances on the kymograph, respectively. Microtubule growth rate was determined as a ratio of these values. Catastrophe frequency was calculated as the inverse growth time. Depolymerization events shorter than 0.5 μm and “catching up” events were considered as short growth perturbation events. Short growth perturbations including “catching up” events were considered as catastrophes when measuring catastrophe frequency. Two or more independent in vitro assays were performed for each reported experiment.

Quantification of EB3 and Fchitax-3 intensity time traces

For the analysis, experiments were performed with 15 μM tubulin, 20 nM mCherry-EB3 and 100 nM Fchitax-3 in the presence of GMPCPP seeds (mismatch conditions) or Fchitax-3 seeds (matching conditions). This analysis was performed similarly to the procedure described in²², apart from time trace alignment. Briefly, simultaneous two-color imaging of Fchitax-3/mCherry-EB3 was performed using an OptoSplit III beamsplitter (Cairn Research Ltd, UK) equipped with double emission filter cube projecting two channels on the camera chip simultaneously. Chromatic aberrations were corrected as described previously using calibration photomask³⁷. Registered videos were used to create kymographs by drawing segmented lines of 10-15 pixel width (0.65-1 μm) along episodes of drug accumulation on growing microtubules using KymoResliceWide plugin with maximum transverse intensity (<http://fiji.sc/KymoResliceWide>).

On extracted kymographs, we outlined rectangular regions of interest (ROI) around observed accumulation event and exported both intensities to MATLAB. For each time point, we fitted mCherry-EB3 profile with sum of constant (lattice binding) and exponential decay functions (comet) convoluted with microscope's point spread function (PSF):

$$I(x) = I_{BG} + \frac{1}{2} I_{lattice} \cdot \operatorname{erfc}\left(\frac{x - x_c}{\sqrt{2}\sigma_{PSF}}\right) + \frac{1}{2} I_{EB} \cdot \exp\left(\frac{\lambda}{2}(\sigma_{PSF}^2 \lambda + 2(x - x_c))\right) \cdot \left(1 - \operatorname{erf}\left(\frac{\sigma_{PSF}^2 \lambda + x - x_c}{\sqrt{2}\sigma_{PSF}}\right)\right)$$

where fitting parameter I_{BG} corresponds to the intensity of background, $I_{lattice}$ to the amplitude of the fluorescence intensity fraction associated with the lattice binding, I_{EB} to the amplitude of convolved exponential decay, x_c to the position of the maximum number of molecules in the molecules distribution (start of exponential decay position), σ_{PSF} to the standard deviation of microscope's PSF and λ to the exponential decay constant. From the fitted function at each time frame we obtained maximum fluorescent intensity $I_{EB_MAX}(t)$.

Intensity of Fchitax-3 was fitted using Gaussian function of variable width with the addition of background. Total intensity was calculated as an integrated area under the fitted curve (without background intensity) and provided $I_{Fchitax3}(t)$. Both $I_{EB_MAX}(t)$ and $I_{Fchitax3}(t)$ intensity traces were normalized by the average of trace values above 80% percentile.

As a reference alignment, we chose Fchitax-3 channel for the time trace averaging, due to its clearly defined shape, and the EB3 time trace for each kymograph was shifted accordingly. Fchitax-3 traces were aligned using normalized cross-correlation. This pairwise function reports similarity between two time profiles depending on the displacement of one relative to another. It provides values in the range between zero and one, where higher values correspond to higher

similarity. The global optimal alignment can be defined as a maximum of sum of cross-correlations between all profile pairs considering all possible displacements combinations. The number of combinations grows exponentially with the number of time traces and we found that time needed to explore the whole parameter space was too long for our datasets. Therefore, we devised an alternative algorithm searching for a local optimal alignment. We chose one time trace as a reference and registered all other time profiles to it, ensuring maximum of cross-correlation in each case. We repeated this procedure for all other time traces serving as a reference, and at the end chose the alignment with the maximum sum of cross-correlation functions among them. We observed that independent of the chosen reference profile, the majority of alignments provided very similar results with comparable cross-correlation score. This can be attributed to a distinctive sigmoid shape of Fchitax-3 time accumulation, making cross-correlation alignment converge to the same set of displacements. The corresponding MATLAB code performing the alignment and averaging, together with kymographs and ROIs used for the described analysis are available online (<https://doi.org/10.6084/m9.figshare.c.5287663>).

Quantification of microtubule tip tapering and EB3 comet intensity

Experiments were performed with GMPCPP seeds in the presence of 15 μM tubulin supplemented with 6.7% HiLyte 488TM labeled tubulin and 20 nM mCherry-EB3 (control, microtubule outgrowth from seeds) or the same mixture supplemented with 100 nM Discodermolide (mismatch conditions, microtubule outgrowth from stable rescue sites). Two-color imaging of HiLyte 488TM labeled tubulin and mCherry-EB3, chromatic aberration correction of movies and kymographs generation were performed in the same way as described in the previous section. EB3 comet traces during episodes of growth ending with a catastrophe were manually outlined with polyline ROI, serving as initial estimation of a position. For each time

point, intensity of HiLyte 488TM labeled tubulin channel was fitted with the error function and background value:

$$I(x) = I_{BG} + \frac{1}{2} I_{\text{tubulin}} \cdot \text{erf}\left(\frac{x - x_c}{\sqrt{2}\sigma_T}\right)$$

where fitting parameter I_{BG} corresponds to the intensity of background, I_{tubulin} to the amplitude of the fluorescent signal along microtubule, x_c to the position of the microtubule tip and σ_T to the degree of tip tapering convolved with microscope's PSF. For the EB3 channel, maximum intensity of fitted comet $I_{EB_MAX}(t)$ was obtained as described in the previous paragraph. EB3 comet time trace was normalized by the average peak intensity over last 20 seconds before the catastrophe after smoothing it with 2.5s interval. The corresponding MATLAB code, kymographs and ROIs used for this analysis are available online (<https://doi.org/10.6084/m9.figshare.c.5287663>).

Single molecule intensity analysis

To estimate fluorescence intensity of single molecules of Fchitax-3, two parallel flow chambers were made on the same coverslip. In one chamber, regular microtubule dynamics assay in the presence of GMPCPP stabilized microtubule seeds with tubulin, mCherry-EB3 and Fchitax-3 was performed. The other chamber was incubated with the same concentration of Fchitax-3 without the reaction mixture. In both conditions, the first 10-20 images of unexposed coverslip areas were acquired with the 100 ms exposure time using low laser intensity and then a movie of 10-20 frames exposing the same area with continuous laser illumination was recorded to induce photobleaching of Fchitax-3 molecules. Fluorescence intensities of Fchitax-3 molecules binding to the coverslip in both chambers were detected and measured using ImageJ plugin DoM_Utrecht v.0.9.1 (https://github.com/ekatruxha/DoM_Utrecht). The fitted peak intensity values were used

to build fluorescence intensity histograms, which were compared to the intensity of Fchitax-3 signal on microtubules.

Laser ablation of microtubules in vitro

Photoablation assays were performed on the TIRF microscope which was equipped with an ILas system (Roper Scientific France/PICT-IBiSA) and a 532 nm Q-switched pulsed laser (Teem Photonics). In vitro microtubule dynamics assay was performed in the presence of GMPCPP stabilized microtubule seeds with 15 μ M tubulin supplemented with 3% rhodamine-tubulin, 20 nM mCherry-EB3 without or with 100 nM Fchitax-3. Control microtubules were severed randomly by 532 nm focused laser beam. In mismatching conditions (GMPCPP seeds extended in presence of 100 nM Fchitax-3), microtubule lattices were ablated at the site of Fchitax-3 accumulations or in the region between the seed and an Fchitax-3 accumulation.

Statistical analysis

GraphPad Prism 7 was used to plot all the histograms and statistical analysis was done using non-parametric Mann-Whitney U-test. For Fig.4b, two-sided Fisher's exact test was performed.

Data and software availability

All data that support the conclusions are available in the manuscript and/or available from the authors on request.

References

1. Desai, A. & Mitchison, T.J. Microtubule polymerization dynamics. *Annu Rev Cell Dev Biol* **13**, 83-117 (1997).
2. Akhmanova, A. & Steinmetz, M.O. Control of microtubule organization and dynamics: two ends in the limelight. *Nat Rev Mol Cell Biol* **16**, 711-726 (2015).
3. Gardner, M.K., Zanic, M. & Howard, J. Microtubule catastrophe and rescue. *Curr Opin Cell Biol* **25**, 14-22 (2013).
4. Aher, A. & Akhmanova, A. Tipping microtubule dynamics, one protofilament at a time. *Curr Opin Cell Biol* **50**, 86-93 (2018).
5. Odde, D.J., Cassimeris, L. & Buettner, H.M. Kinetics of microtubule catastrophe assessed by probabilistic analysis. *Biophys J* **69**, 796-802 (1995).
6. Gardner, M.K., Zanic, M., Gell, C., Bormuth, V. & Howard, J. The depolymerizing kinesins Kip3 (kinesin-8) and MCAK (kinesin-13) are catastrophe factors that destabilize microtubules by different mechanisms. *Cell* **147**, 1092-1103 (2011).
7. Coombes, C.E., Yamamoto, A., Kenzie, M.R., Odde, D.J. & Gardner, M.K. Evolving tip structures can explain age-dependent microtubule catastrophe. *Curr Biol* **23**, 1342-1348 (2013).
8. Doodhi, H. *et al.* Termination of Protofilament Elongation by Eribulin Induces Lattice Defects that Promote Microtubule Catastrophes. *Curr Biol* **26**, 1713-1721 (2016).
9. Duellberg, C., Cade, N.I. & Surrey, T. Microtubule aging probed by microfluidics-assisted tubulin washout. *Mol Biol Cell* **27**, 3563-3573 (2016).
10. Chretien, D. & Fuller, S.D. Microtubules switch occasionally into unfavorable configurations during elongation. *J Mol Biol* **298**, 663-676 (2000).

11. Chaaban, S. & Brouhard, G.J. A microtubule bestiary: structural diversity in tubulin polymers. *Mol Biol Cell* **28**, 2924-2931 (2017).
12. Cross, R.A. Microtubule lattice plasticity. *Curr Opin Cell Biol* **56**, 88-93 (2018).
13. Chretien, D., Metz, F., Verde, F., Karsenti, E. & Wade, R.H. Lattice defects in microtubules: protofilament numbers vary within individual microtubules. *J Cell Biol* **117**, 1031-1040 (1992).
14. Arnal, I. & Wade, R.H. How does taxol stabilize microtubules? *Curr Biol* **5**, 900-908 (1995).
15. Atherton, J., Stouffer, M., Francis, F. & Moores, C.A. Microtubule architecture in vitro and in cells revealed by cryo-electron tomography. *Acta Crystallogr D Struct Biol* **74**, 572-584 (2018).
16. Vitre, B. *et al.* EB1 regulates microtubule dynamics and tubulin sheet closure in vitro. *Nat Cell Biol* **10**, 415-421 (2008).
17. Schaedel, L. *et al.* Lattice defects induce microtubule self-renewal *Nat Physics* **15**, 830-838 (2019).
18. Schaedel, L. *et al.* Microtubules self-repair in response to mechanical stress. *Nat Mater* **14**, 1156-1163 (2015).
19. Aumeier, C. *et al.* Self-repair promotes microtubule rescue. *Nat Cell Biol* **18**, 1054-1064 (2016).
20. Dimitrov, A. *et al.* Detection of GTP-tubulin conformation in vivo reveals a role for GTP remnants in microtubule rescues. *Science* **322**, 1353-1356 (2008).
21. Brouhard, G.J. & Rice, L.M. Microtubule dynamics: an interplay of biochemistry and mechanics. *Nat Rev Mol Cell Biol* **19**, 451-463 (2018).

22. Rai, A. *et al.* Taxanes convert regions of perturbed microtubule growth into rescue sites. *Nat Mater* **19**, 355-365 (2020).
23. Zanic, M., Stear, J.H., Hyman, A.A. & Howard, J. EB1 recognizes the nucleotide state of tubulin in the microtubule lattice. *PLoS One* **4**, e7585 (2009).
24. Maurer, S.P., Fourniol, F.J., Bohner, G., Moores, C.A. & Surrey, T. EBs recognize a nucleotide-dependent structural cap at growing microtubule ends. *Cell* **149**, 371-382 (2012).
25. Duellberg, C., Cade, N.I., Holmes, D. & Surrey, T. The size of the EB cap determines instantaneous microtubule stability. *Elife* **5**, e13470 (2016).
26. Roostalu, J. *et al.* The speed of GTP hydrolysis determines GTP cap size and controls microtubule stability. *Elife* **9**, e51992 (2020).
27. Diaz, J.F., Valpuesta, J.M., Chacon, P., Diakun, G. & Andreu, J.M. Changes in microtubule protofilament number induced by Taxol binding to an easily accessible site. Internal microtubule dynamics. *J Biol Chem* **273**, 33803-33810 (1998).
28. Estevez-Gallego, J. *et al.* Structural model for differential cap maturation at growing microtubule ends. *Elife* **9**, e50155 (2020).
29. Matesanz, R. *et al.* Modulation of microtubule interprotofilament interactions by modified taxanes. *Biophys J* **101**, 2970-2980 (2011).
30. Ginsburg, A. *et al.* Structure of Dynamic, Taxol-Stabilized, and GMPPCP-Stabilized Microtubule. *J Phys Chem B* **121**, 8427-8436 (2017).
31. Hyman, A.A., Chretien, D., Arnal, I. & Wade, R.H. Structural changes accompanying GTP hydrolysis in microtubules: information from a slowly hydrolyzable analogue guanylyl-(alpha,beta)-methylene-diphosphonate. *J Cell Biol* **128**, 117-125 (1995).

32. Andreu, J.M. *et al.* Solution structure of Taxotere-induced microtubules to 3-nm resolution. The change in protofilament number is linked to the binding of the taxol side chain. *J Biol Chem* **269**, 31785-31792 (1994).
33. Andreu, J.M. *et al.* Low resolution structure of microtubules in solution. Synchrotron X-ray scattering and electron microscopy of taxol-induced microtubules assembled from purified tubulin in comparison with glycerol and MAP-induced microtubules. *J Mol Biol* **226**, 169-184 (1992).
34. Bieling, P. *et al.* Reconstitution of a microtubule plus-end tracking system in vitro. *Nature* **450**, 1100-1105 (2007).
35. Mohan, R. *et al.* End-binding proteins sensitize microtubules to the action of microtubule-targeting agents. *Proc Natl Acad Sci U S A* **110**, 8900-8905 (2013).
36. Komarova, Y. *et al.* Mammalian end binding proteins control persistent microtubule growth. *J Cell Biol* **184**, 691-706 (2009).
37. Aher, A. *et al.* CLASP Suppresses Microtubule Catastrophes through a Single TOG Domain. *Dev Cell* **46**, 40-58 (2018).
38. Debs, G.E., Cha, M., Liu, X., Huehn, A.R. & Sindelar, C.V. Dynamic and asymmetric fluctuations in the microtubule wall captured by high-resolution cryoelectron microscopy. *Proc Natl Acad Sci U S A* **117**, 16976-16984 (2020).
39. Zhang, R., LaFrance, B. & Nogales, E. Separating the effects of nucleotide and EB binding on microtubule structure. *Proc Natl Acad Sci U S A* **115**, E6191-E6200 (2018).
40. Zhang, R., Alushin, G.M., Brown, A. & Nogales, E. Mechanistic Origin of Microtubule Dynamic Instability and Its Modulation by EB Proteins. *Cell* **162**, 849-859 (2015).
41. Shima, T. *et al.* Kinesin-binding-triggered conformation switching of microtubules contributes to polarized transport. *J Cell Biol* **217**, 4164-4183 (2018).

42. Zakharov, P. *et al.* Molecular and Mechanical Causes of Microtubule Catastrophe and Aging. *Biophys J* **109**, 2574-2591 (2015).
43. Vemu, A. *et al.* Severing enzymes amplify microtubule arrays through lattice GTP-tubulin incorporation. *Science* **361**, eaau1504 (2018).
44. Diaz, J.F. & Andreu, J.M. Assembly of purified GDP-tubulin into microtubules induced by taxol and taxotere: reversibility, ligand stoichiometry, and competition. *Biochemistry* **32**, 2747-2755 (1993).
45. Li, X., Barasoain, I., Matesanz, R., Diaz, J.F. & Fang, W.S. Synthesis and biological activities of high affinity taxane-based fluorescent probes. *Bioorg Med Chem Lett* **19**, 751-754 (2009).
46. Paterson, I., Florence, G.J., Gerlach, K., Scott, J.P. & Sereinig, N. A practical synthesis of (+)-discodermolide and analogues: fragment union by complex aldol reactions. *J Am Chem Soc* **123**, 9535-9544 (2001).
47. Kamimura, S., Fujita, Y., Wada, Y., Yagi, T. & Iwamoto, H. X-ray fiber diffraction analysis shows dynamic changes in axial tubulin repeats in native microtubules depending on paclitaxel content, temperature and GTP-hydrolysis. *Cytoskeleton (Hoboken)* **73**, 131-144 (2016).
48. Estevez-Gallego, J. *et al.* Structural model for differential cap maturation at growing microtubule ends. *Elife* **9** (2020).
49. Matesanz, R. *et al.* Taxanes with high potency inducing tubulin assembly overcome tumoural cell resistances. *Bioorg Med Chem* **22**, 5078-5090 (2014).
50. Zheng, S.Q. *et al.* MotionCor2: anisotropic correction of beam-induced motion for improved cryo-electron microscopy. *Nat Methods* **14**, 331-332 (2017).

Acknowledgements

We thank G. F. Díaz for calf brains supply and staff of beamline BL11-NCD-SWEET (ALBA, Cerdanyola del Vallès, Spain) for their support with X-ray fiber diffraction experiment. We thank S. Kamimura (Chuo University, Tokyo, Japan) for kindly providing the share-flow device employed for fiber diffraction experiments. We thank W. S. Fang for kindly providing Fchitax-3, S. Glauser and K.-H. Altmann for kindly providing Alexia₄₈₈-Epothilone B. This work was supported by the European Research Council Synergy grant 609822 and the Netherlands Organization for Scientific Research (NWO) CW ECHO grant 711.015.005 to A.A., by a Biotechnology and Biological Sciences Research Council (BBSRC, BB/N018176/1) grant to C.A.M., and by grants "Bases moleculares de la regulación de microtúbulos y sus implicaciones en la neurotoxicidad producida por fármacos" from Fundación TATIANA, 20202020E301 from CSIC and PID2019-104545RB-I00 from Ministerio de Ciencia, Innovación y Universidades to J.F.D.

Author Contributions

A.R. designed and performed experiments, analyzed data and wrote the paper. T.L. and C.A.M designed and performed cryo-EM experiments and analyzed the data; E.A. analyzed data; J.E.G. and J.F.D. performed X-ray fiber diffraction experiments; I.P. provided synthetic discodermolide; L.C.K contributed to the design of the experiments and analysis of the data and models; A.A. designed experiments, coordinated the project and wrote the paper.

Competing financial interests

The authors declare no competing financial interests.

Figure legends

Figure 1. Microtubule protofilament number affects microtubule growth rate.

a) X-ray fiber diffraction measurements for protofilament (pf) number quantification of microtubules polymerized in the presence of GMPCPP or different MSAs. For each condition, a total of 24 diffraction images were averaged and background subtracted using ImageJ software.

b) Representative raw cryo-EM images (in the presence of Taxol, GMPCPP and Fchitax-3) and their filtered versions emphasizing their Moiré patterns. Scale bar, 25 nm. Bar graph shows microtubule protofilament number distribution for different conditions determined by Moiré pattern visualization for each microtubule. Microtubule population: $n = 89$ for Taxol; $n = 52$ for GMPCPP; $n = 77$ for Fchitax-3.

c) Representative kymographs showing microtubule dynamics in the presence of seeds (stabilized with GMPCPP or indicated MSAs) with different protofilament numbers, supplemented with tubulin (15 μ M) and mCherry-EB3 (20 nM) in the absence of any additional MSAs added during the reaction.

d, e) Quantification of growth rates (**d**) and catastrophe frequencies (**e**) in the presence of seeds with different protofilament numbers as presented in panel **c**. From left to right, $n = 100, 113, 82, 81, 76, 60$ growth events. $N = 2$ independent experiments for Docetaxel and Alexa₄₈₈-Epothilone B, $N = 3$ independent experiments for Taxol, GMPCPP and Fchitax-3. Error bars represent SD; ***, $p < 0.001$, ****, $p < 0.0001$, Mann-Whitney U test.

Figure 2. Protofilament number mismatch between the seed and growth conditions affects microtubule dynamics.

a) A scheme illustrating microtubule growth from seeds in the presence of MSAs with the same or different protofilament number preference.

b) (Left) A cartoon depicting kymographs that correspond to three different types of microtubule dynamics observed in different conditions. (Right); Quantification of microtubule dynamics observed in the indicated conditions, as represented in the cartoon and in panel (c). $n = 75$ microtubule seeds in all the conditions, $N = 3$ independent experiments.

c) Representative kymographs showing microtubule dynamics in the indicated conditions. Short growth perturbation events followed by rapid rescues are highlighted in the Taxol panel (white asterisk highlights a split comet and a yellow asterisk highlights a depolymerization event shorter than $0.5 \mu\text{m}$). Stable rescue sites in mismatching conditions are highlighted by white stippled lines. $N = 3$ independent experiments.

d-f) Representative kymographs illustrating microtubule dynamics in different conditions, as indicated.

Figure 3. Extent of MSA accumulation at pre-catastrophe microtubule tips depends on the match between the seed and growth conditions.

a, b) Representative kymographs illustrating drug accumulations in mismatching conditions. Microtubules were grown from GMPCPP seeds (a) or Taxol seeds (b) in the presence of $15 \mu\text{M}$ tubulin and 20 nM mCherry-EB3 with Fchitax-3 (100 nM) (a) or Alexa₄₈₈-Epothilone B (100 nM) (b). White arrows indicate stable rescue sites with drug accumulations.

c, d) Representative kymographs illustrating drug accumulations in matching conditions. Microtubules were grown from GMPCPP seeds (c) or Fchitax-3 seeds (d) in the presence of $15 \mu\text{M}$ tubulin and 20 nM mCherry-EB3 with Alexa₄₈₈-Epothilone B (100 nM) (c) or Fchitax-3 (100 nM) (d). Split comets are indicated with white arrows.

e) Quantification of drug accumulation lengths in the indicated conditions. Error bars indicate SD; from left to right, $n = 39, 34, 30$ and 50 , $N = 3$ independent experiments, ***, $p < 0.001$.

f) Time plot of averaged normalized maximum intensity of fitted EB3 comet (orange, red) and normalized area under the curve of fitted Fchitax-3 (light and dark green) intensity profiles in mismatching conditions (as shown in panel a, $n = 9$ kymographs from 5 experiments) and in matching conditions (as shown in panel d, $n = 38$ kymographs from 5 experiments). Individual curves were aligned by maximizing cross-correlation between Fchitax-3 time curves. Error bars represent SEM.

g) Frequencies of catastrophes and split comet events in different matching conditions. From left to right, $n = 65, 100, 91, 71,$ and 70 for catastrophe frequencies for the indicated conditions and $n = 60, 66, 73, 62$ and 63 “catching up” events from 30 microtubules for split comet frequencies. $N = 3$ independent experiments. Error bars represent SD.

Figure 4. Lattice defects observed in mismatching conditions are associated with switching of protofilament number.

a, c) Quantification of growth rates (a) and catastrophe frequencies (c) for the indicated conditions. For better comparison, data from Fig. 1d and 1e are presented again in the present panels. $n = 100, 113, 82, 60$ microtubule growth events for microtubules polymerized from Taxol, GMPCPP, Docetaxel, Fchitax-3 seeds. $n = 91, 70, 71, 100$ in the presence of Taxol seed + Taxol (100 nM), GMPCPP seed + Docetaxel (100 nM), Docetaxel seed + Docetaxel (100 nM), Fchitax-3 seed + Fchitax-3 (100 nM). $n = 30$ and 40 for Taxol seed + Fchitax-3 (100 nM) before and after stable rescue site (SRS) formation. $n = 60$ and 75 for GMPCPP seed + Fchitax-3 (100 nM) before and after SRS formation. $n = 35$ and 51 for GMPCPP seed + Taxol (100 nM) before and after SRS formation. $N = 3$ independent experiments. Error bars represent SD. The colors of the bars and *p* values indicate the protofilament number preferences of a particular drug used.

b) Representative raw cryo-EM images and their filtered versions with enhanced microtubule Moiré patterns showing the diameter difference (pf number transition) for microtubules grown from GMPCPP seeds in the presence of Fchitax-3 (mismatching condition, Fig. 3a). The left and central sets of panels show defect-containing microtubules and the right one shows a microtubule with no visible defects. In each panel, Image 1 is the raw cryo-EM image of one microtubule. Scale bar, 25 nm. Image 2 is the same cryo-EM image with purple, yellow and red dash lines highlighting diameter difference on either side of a defect. Image 3 shows the diameters for two sides of microtubule. Diameters were measured in Fiji. Percentage of microtubule with protofilament number transition in microtubules with no visible defects ($n = 19$) and microtubules with sheet-like defects ($n = 17$). The percentage differences were evaluated by two-sided Fisher's exact test. **, p value = 0.0023.

d) Representative kymographs showing occurrence of a second stable rescue site (SRS) after the formation of the first SRS within the same microtubule. The experiment was performed with GMPCPP seeds in the presence of 15 μ M tubulin, 20 nM EB3 and 100 nM Fchitax-3. Bar graph shows quantification of microtubule growth rates before ($n = 60$) and after the first ($n = 75$) and the second ($n = 53$) stable rescue site. $N = 3$ independent experiments, ns = not significant, ***, $p < 0.001$, Mann-Whitney U test.

e) Bar graphs show quantification of frequency of drug accumulations at pre-catastrophe microtubule ends growing either from a seed or after a stable rescue site (SRS). Left panel: quantification of catastrophes from all microtubule seeds (with and without drug binding). Right panel: quantification of catastrophes only for microtubules showing drug binding. In case of SRS, only microtubules showing two consecutive stable rescue sites were included.

f, g) The degree of microtubule tip tapering (f) (derived from the fit to error function, with higher values corresponding to higher tapering) and averaged normalized maximum intensity of fitted

EB3 comet (g) aligned by the moment of catastrophe. Black curves correspond to microtubules growing from seeds in control conditions (15 μ M tubulin supplemented with 6.7% green tubulin, 20 nM mCherry-EB3 in the presence of GMPCPP seeds, 73 kymographs from 5 experiments). Red curves correspond to growth events from stable rescue sites (15 μ M tubulin supplemented with 6.7% green tubulin, 20 nM mCherry-EB3 and 100 nM Discodermolide in the presence of GMPCPP seed, 64 kymographs from 5 experiments). Error bars represent SEM.

Figure 5. Microtubule severing at the stable rescue site suppresses catastrophes.

a) Schematic representation of a microtubule severing experiment using 532 nm laser. Microtubule regions were severed within drug accumulation area (i) or before drug accumulation area (ii). Growth patterns of severed microtubule parts in both conditions were analyzed as represented in the cartoon kymographs.

b, d) Still images showing the photoablation of microtubule regions within (b) or before (d) drug accumulation area (SRS) and microtubule dynamics of the severed parts. The severed regions and microtubule plus ends are indicated. Asterisks show the positions of the GMPCPP seeds. Kymographs illustrate growth of the severed microtubule fragments (N = 5 independent experiments).

c) Quantification of growth dynamics of the severed microtubule segment as represented in panels b and d. n = 80 and 55 for severing within and before a drug accumulation area, respectively.

e) Catastrophe frequencies of microtubules growing in matching conditions (Fchitax-3 seeds + 100 nM Fchitax-3, n = 100), after the formation of stable rescue sites in mismatching conditions (GMPCPP seeds + 100 nM Fchitax-3, n= 76), microtubule fragments growing after photoablation within an Fchitax-3 accumulation area (SRS) (n = 39) and microtubule fragments growing after

photoablation in a region preceding the Fchitax-3 accumulation area (SRS) (n = 115) in mismatching conditions.

f) Model depicting microtubule lattice repair in matching and mismatching conditions. In pre-catastrophe state, MSAs stabilize depolymerizing protofilaments and inhibit depolymerization. In matching conditions, this leads to rapid repair of microtubule defects and restoration of normal microtubule growth. In mismatching conditions, lattice defects persist in spite of repair due to a switch in protofilament number. The presence of a defect affects the growing microtubule end and induces catastrophe.

Supplementary Figure legends

Supplementary Figure 1. Effects of microtubule protofilament number on microtubule growth rate.

a) Schematic representation of the in vitro microtubule dynamics assay and cartoons of kymographs illustrating microtubule growth events from a microtubule seed stabilized with GMPCPP or microtubule stabilizing agents (MSAs).

b) Representative kymographs showing microtubule dynamics in the presence of seeds (stabilized with GMPCPP or the indicated drugs) with different protofilament numbers in the presence of tubulin (15 μ M supplemented with 3% of rhodamine tubulin) in the absence of EB3 and without additional MSAs added during the reaction.

c, d) Quantification of growth rates (c) and catastrophe frequencies (d) in the presence of seeds with different protofilament numbers as presented in panel b. From left to right, $n = 52, 82, 62, 62, 51, 60$ growth events. $N = 3$ independent experiments for Taxol, GMPCPP and Fchitax-3-microtubule seeds, $N = 2$ independent experiments for Docetaxel and Alexa488-Epothilone B-microtubule seeds, error bars represent SD; ***, $p < 0.001$, ****, $p < 0.0001$, Mann-Whitney U test.

Supplementary Figure 2. Effects of microtubule protofilament number on microtubule growth and depolymerization rates.

a) Still images and representative kymographs showing the presence of two different kinds of seeds and microtubules growing from these seeds in the same assay. In the upper panel, Taxol (13pf) and GMPCPP (14pf) seeds were mixed (i). In the middle panel, Docetaxel seeds (14pf) were mixed with GMPCPP seeds (14pf) (ii). In the bottom panel GMPCPP seeds (14pf) were mixed with Fchitax-3 seeds (15/16pf) (iii). Respective bar graphs show the quantification of

microtubule growth rate from different seeds during seed mixing conditions. Only growth events originating from seeds (highlighted by yellow arrows) and not from rescue sites were included in the quantification. For better comparison, data from Fig. 1d (“alone”) are included in the present panels. From left to right- n = 100, 40, 113, 40 (panel i), n = 82, 47, 113, 47 (panel ii), n = 113, 66, 60, 60 (panel iii).

b) Representative kymographs showing microtubule depolymerization events as indicated. Bar graph shows the quantification of shortening rates. N = 3 independent experiments, n = 100 for all the conditions, *, p <0.01, Mann-Whitney U test.

Supplementary Figure 3. Effects of protofilament number mismatch between the seed and growth conditions on microtubule dynamics.

a) Representative kymographs showing microtubule dynamics in the indicated conditions. N = 3 independent experiments.

b) Quantification of microtubule dynamics patterns for conditions shown in panel a. n = 50 microtubule seeds in all conditions.

Supplementary Figure 4. Effects of protofilament number mismatch between the seed and growth conditions on microtubule dynamics.

Kymographs showing microtubule dynamics in the absence of EB3 for microtubules polymerized in the indicated conditions.

Supplementary Figure 5. Characterization of microtubule growth perturbations in the presence of MSAs in matching conditions.

a) Representative kymographs illustrating the dynamics of microtubules grown in matching conditions, from Docetaxel seeds in the presence of 15 μ M tubulin and 20 nM mCherry-EB3 with Alexa₄₈₈-Epothilone B (100 nM). White arrows indicate split comets.

b, c) Representative kymographs showing split comets (“catching up” events, white arrows) in matching conditions as indicated.

d) Kymograph illustrating the accumulation of Fchitax-3 molecules at the site of a split comet (inset) and free Fchitax-3 molecules binding to coverslip during the assay. Quantification of the number of Fchitax-3 molecules at the accumulation site is shown on the right.

Supplementary Figure 6. Analysis of changes in protofilament number associated with split comets and lattice defects.

a) Quantification of growth rates before and after a “catching up” event in matching conditions. 20 events were analyzed per condition.

b) A table showing the comparison of microtubule diameter on either side of a defect in microtubules grown from GMPCPP seeds in the presence of Fchitax-3. MTs with diameter difference of ≥ 2 nm were identified as MTs with protofilament number transition.

Figure 1

bioRxiv preprint doi: <https://doi.org/10.1101/2021.02.11.430743>; this version posted February 11, 2021. The copyright holder for this preprint (which was not certified by peer review) is the author/funder, who has granted bioRxiv a license to display the preprint in perpetuity. It is made available under a [CC-BY-NC-ND 4.0 International license](https://creativecommons.org/licenses/by-nc-nd/4.0/).

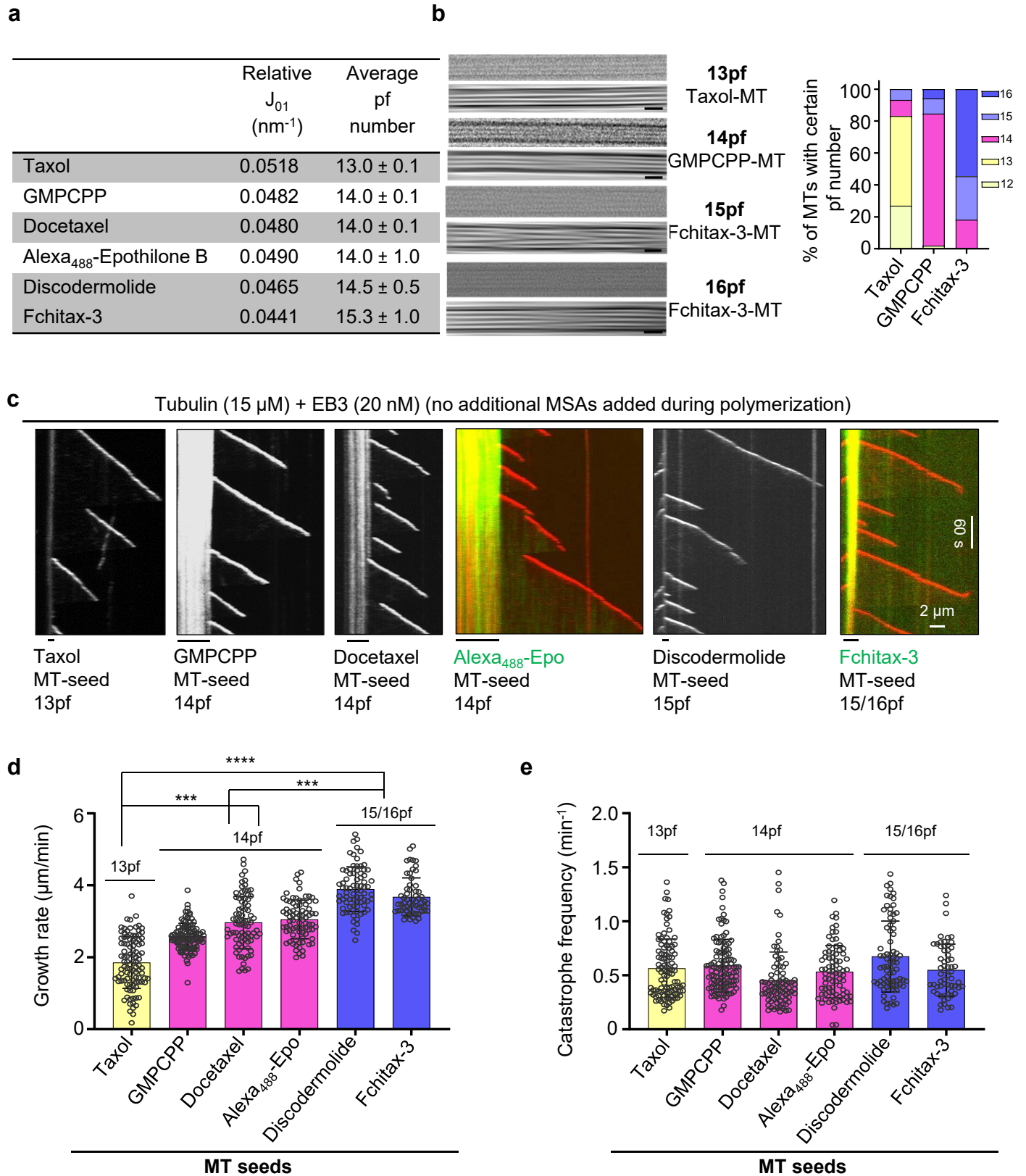


Figure 2

bioRxiv preprint doi: <https://doi.org/10.1101/2021.02.11.430743>; this version posted February 11, 2021. The copyright holder for this preprint (which was not certified by peer review) is the author/funder, who has granted bioRxiv a license to display the preprint in perpetuity. It is made available under a [CC-BY-NC-ND 4.0 International license](https://creativecommons.org/licenses/by-nc-nd/4.0/).

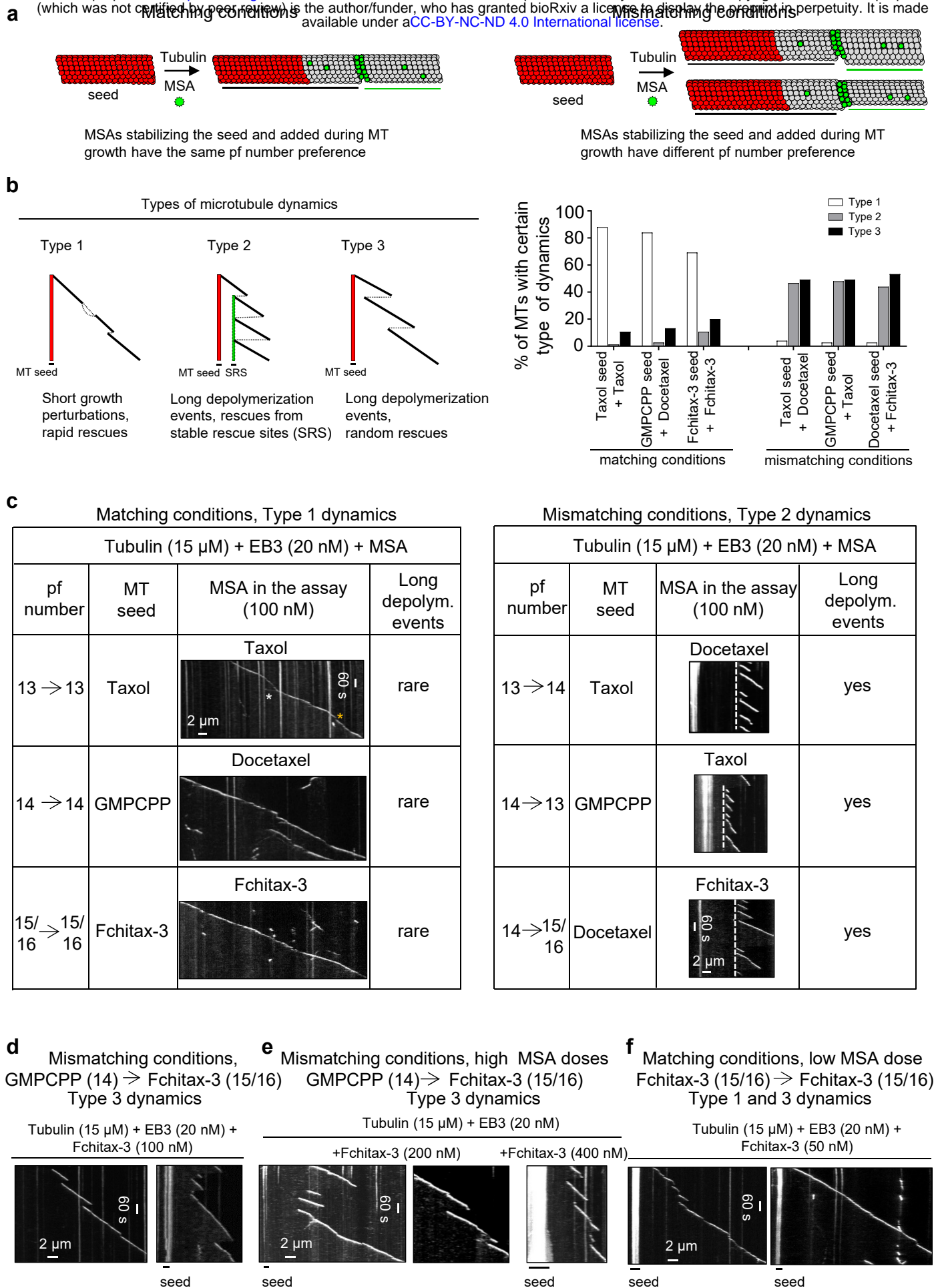


Figure 3

bioRxiv preprint doi: <https://doi.org/10.1101/2021.02.11.430743>; this version posted February 11, 2021. The copyright holder for this preprint (which was not certified by peer review) is the author/funder, who has granted bioRxiv a license to display the preprint in perpetuity. It is made available under aCC-BY-ND 4.0 International license.

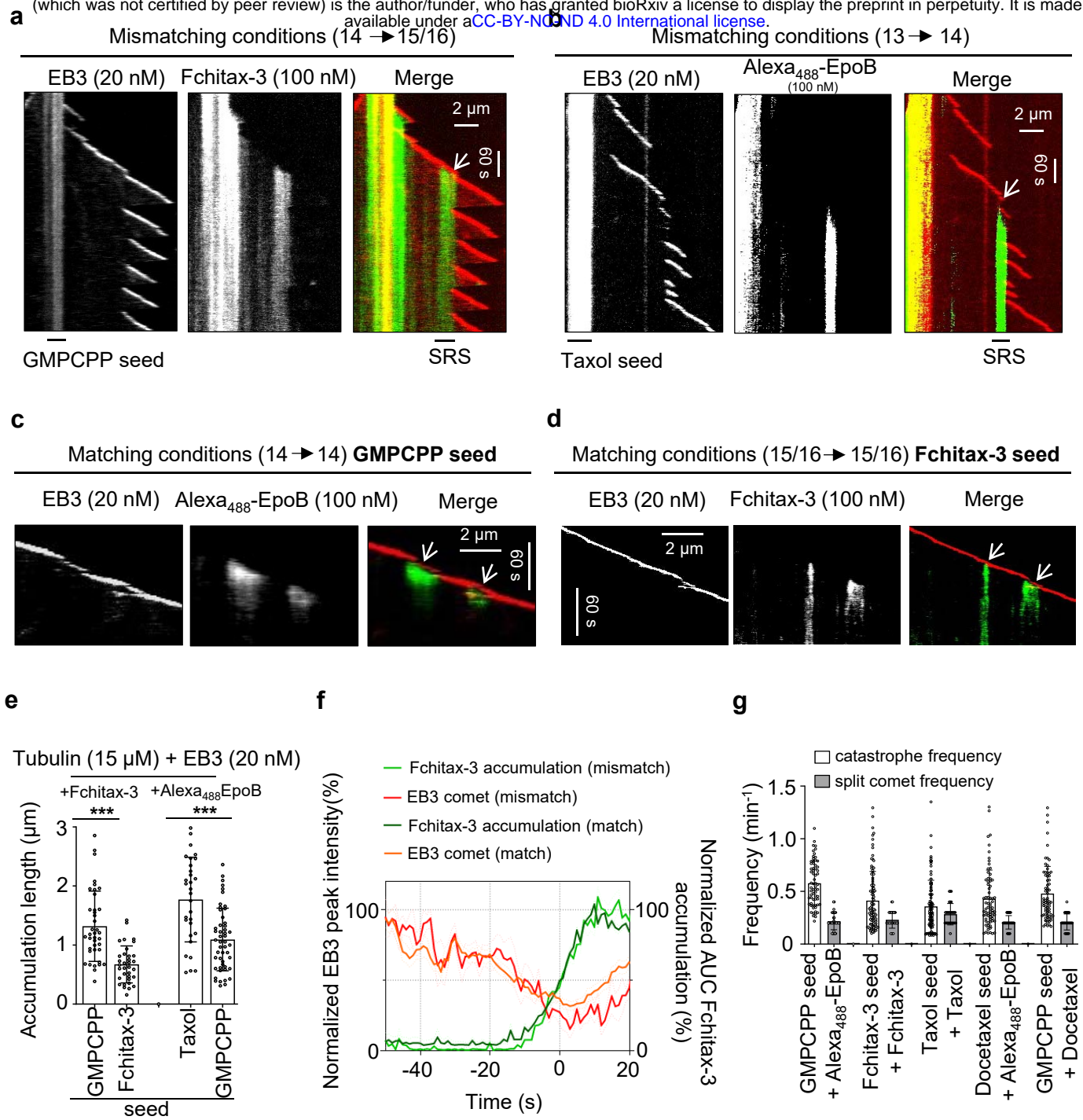


Figure 4

bioRxiv preprint doi: <https://doi.org/10.1101/2021.02.11.430743>; this version posted February 11, 2021. The copyright holder for this preprint (which was not certified by peer review) is the author/funder, who has granted bioRxiv a license to display the preprint in perpetuity. It is made available under aCC-BY-NC-ND 4.0 International license.

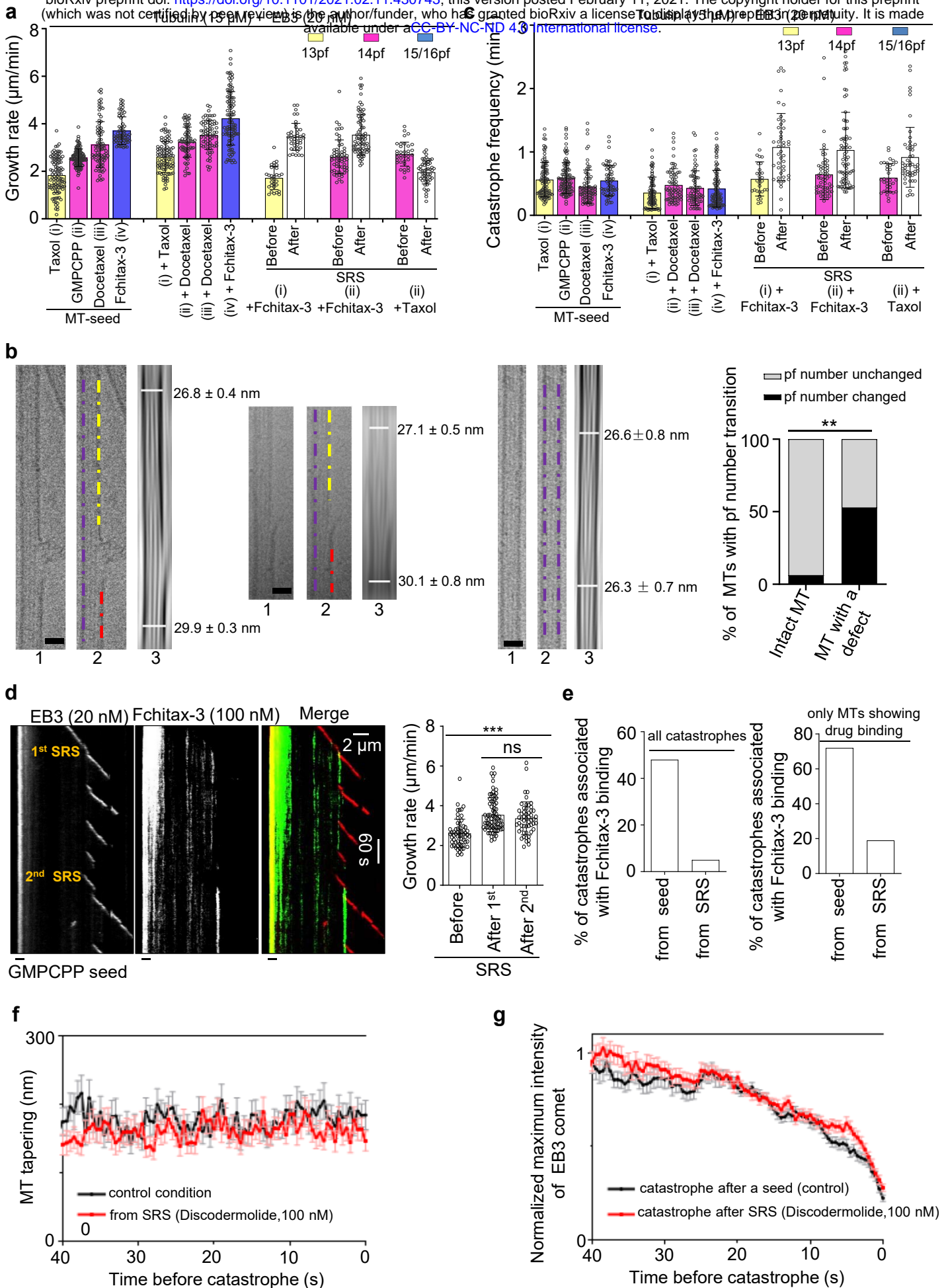
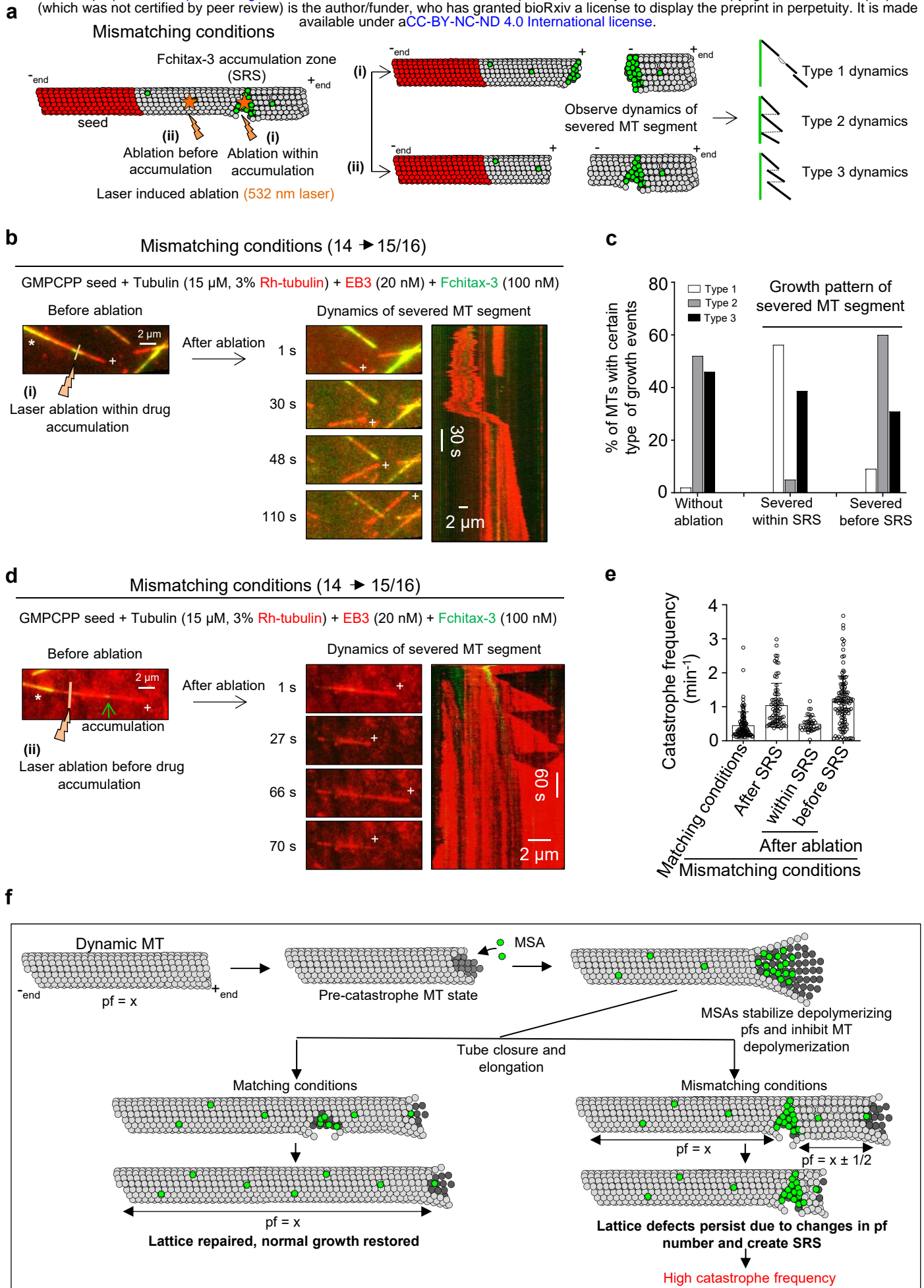


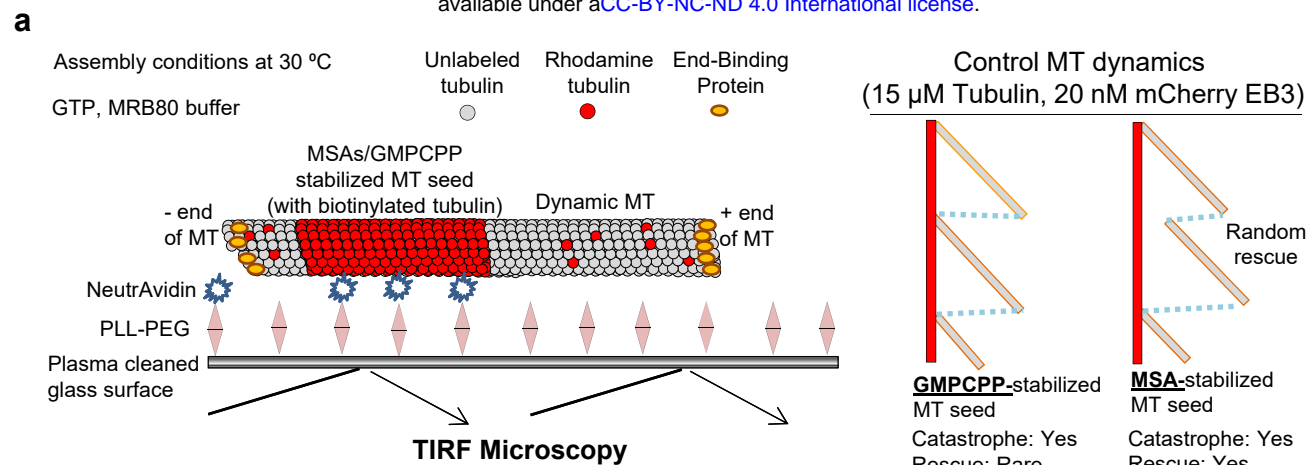
Figure 5

bioRxiv preprint doi: <https://doi.org/10.1101/2021.02.11.430743>; this version posted February 11, 2021. The copyright holder for this preprint (which was not certified by peer review) is the author/funder, who has granted bioRxiv a license to display the preprint in perpetuity. It is made available under a [CC-BY-NC-ND 4.0 International license](#).



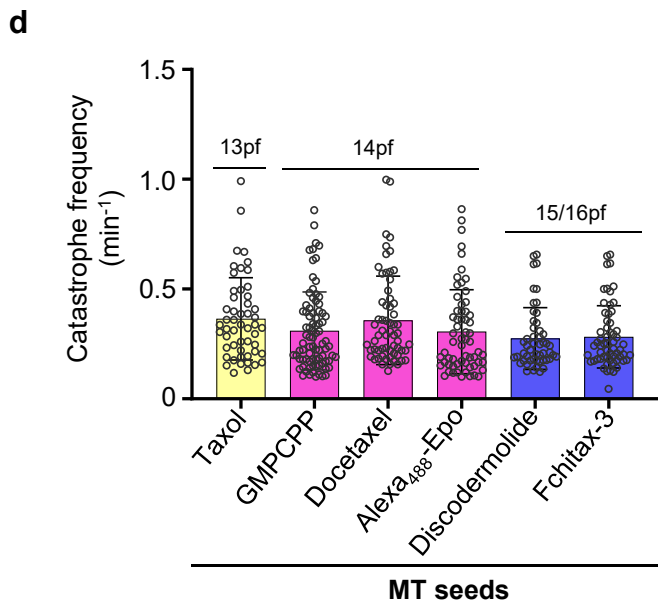
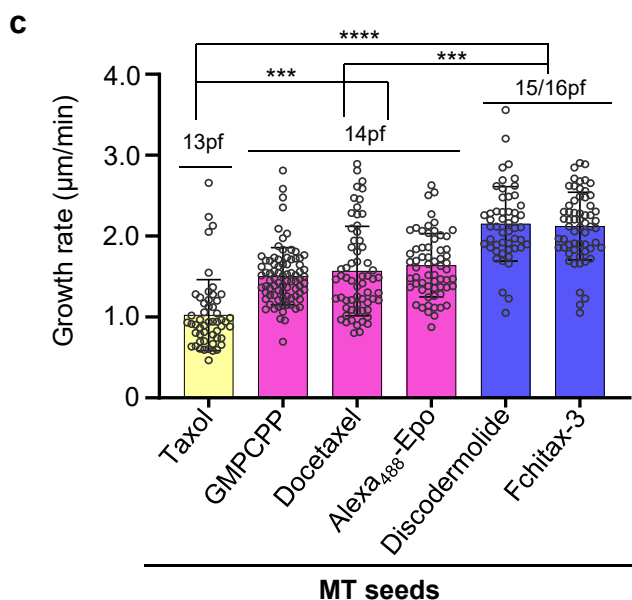
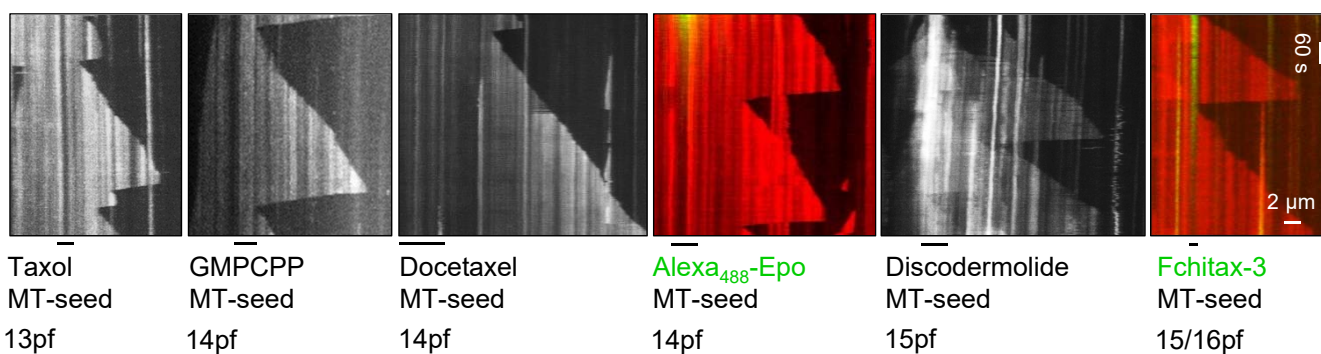
Supplementary Figure 1

bioRxiv preprint doi: <https://doi.org/10.1101/2021.02.11.430743>; this version posted February 11, 2021. The copyright holder for this preprint (which was not certified by peer review) is the author/funder, who has granted bioRxiv a license to display the preprint in perpetuity. It is made available under a [CC-BY-NC-ND 4.0 International license](#).



b

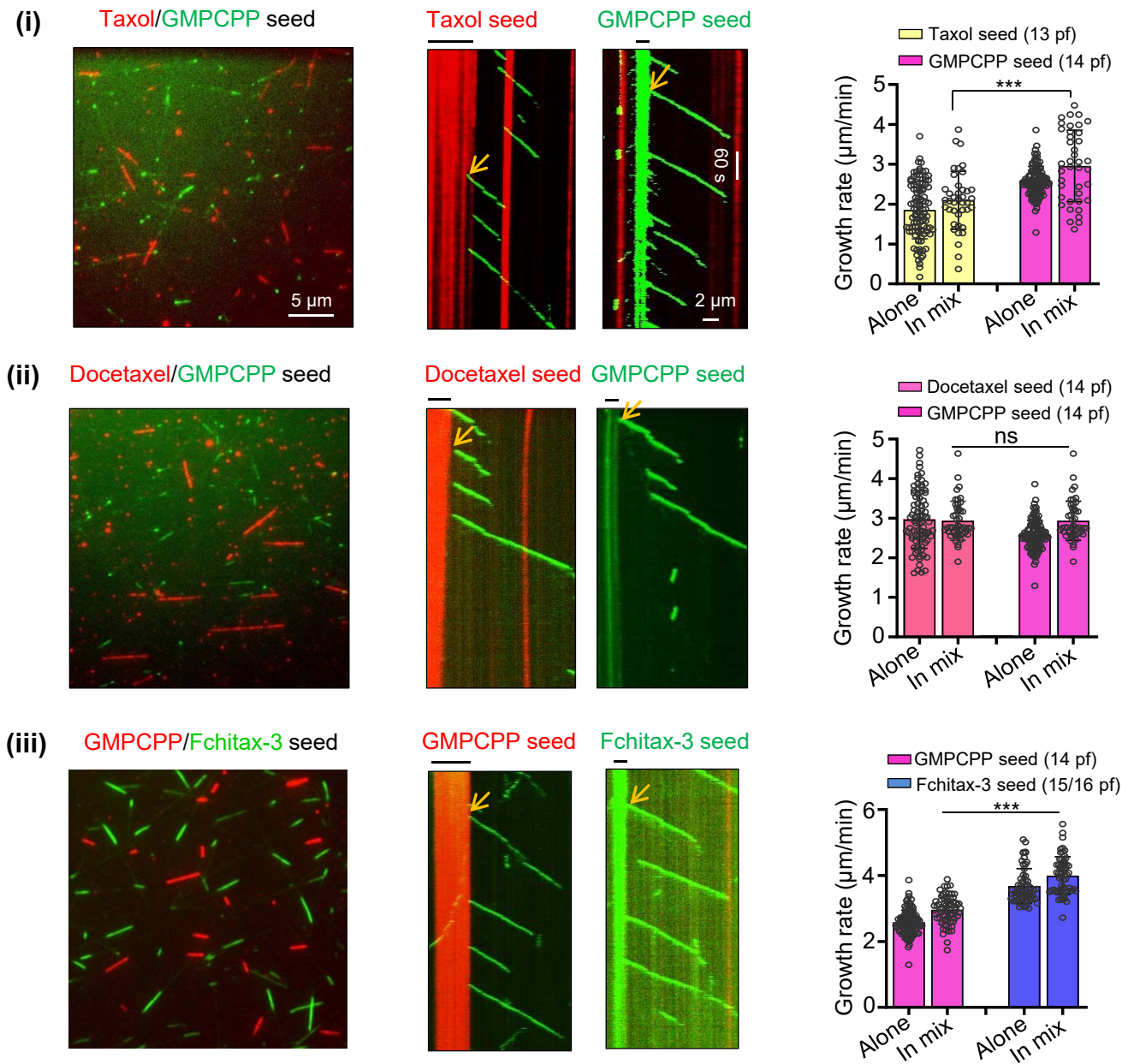
Tubulin (15 μ M) supplemented with 3% Rh-tubulin (no additional MSAs added during polymerization)



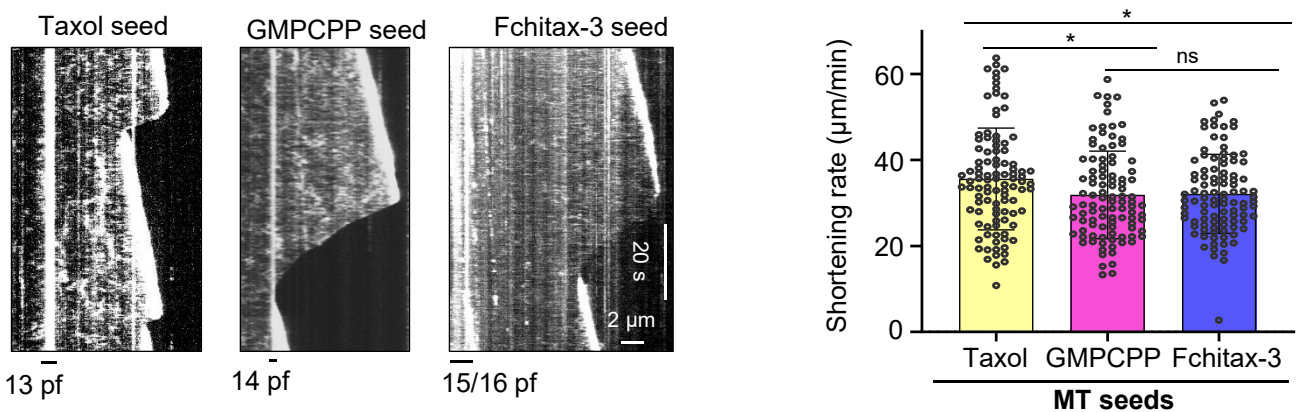
Supplementary Figure 2

bioRxiv preprint doi: <https://doi.org/10.1101/2021.02.11.430743>; this version posted February 11, 2021. The copyright holder for this preprint (which was not certified by peer review) is the author/funder, who has granted bioRxiv a license to display the preprint in perpetuity. It is made available under a [CC-BY-NC-ND 4.0 International license](https://creativecommons.org/licenses/by-nc-nd/4.0/).

a
Tubulin (15 μM) + GFP-EB3 (20 nM) (no additional MSAs added during polymerization)
two types of seeds present in the same assay



b
Tubulin (15 μM) + EB3 (20 nM) (no additional MSAs added during polymerization)



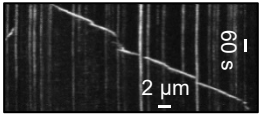
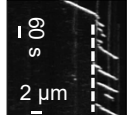
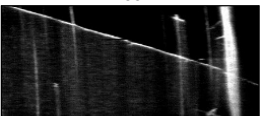
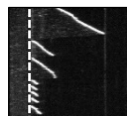
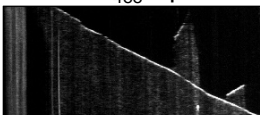
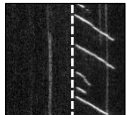
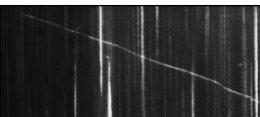
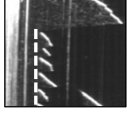
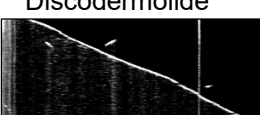

Supplementary Figure 3

bioRxiv preprint doi: <https://doi.org/10.1101/2021.02.11.430743>; this version posted February 11, 2021. The copyright holder for this preprint (which was not certified by peer review) is the author/funder, who has granted bioRxiv a license to display the preprint in perpetuity. It is made available under a [CC-BY-NC-ND 4.0 International license](https://creativecommons.org/licenses/by-nc-nd/4.0/).

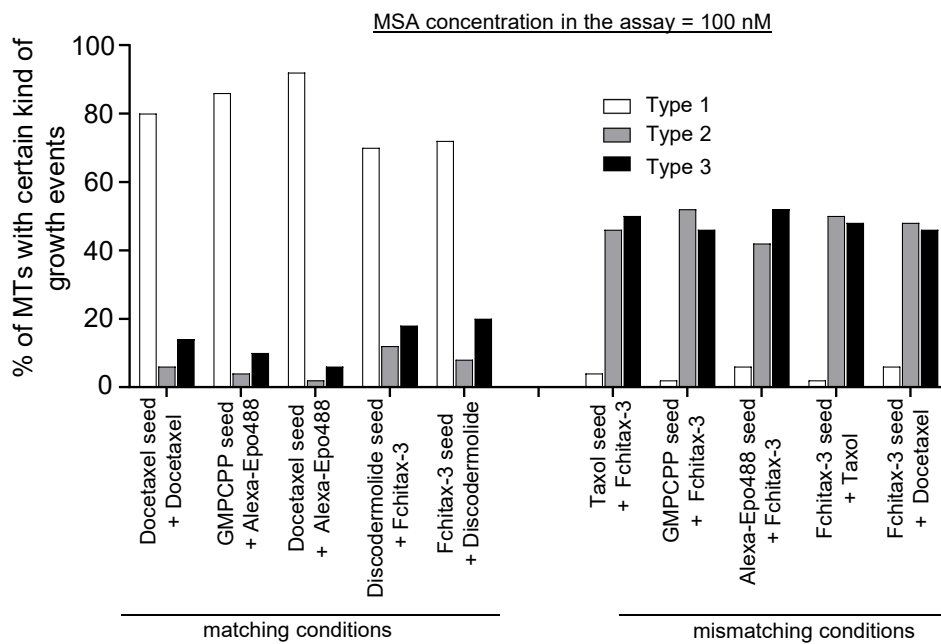
a

Matching conditions, Type 1 dynamics

Mismatching conditions, Type 2 dynamics

Tubulin (15 μ M) + EB3 (20 nM) + MSA				Tubulin (15 μ M) + EB3 (20 nM) + MSA			
pf number	MT Seed	MSA in the assay (100 nM)	Long depolym. events	pf number	MT Seed	MSA in the assay (100 nM)	Long depolym. events
14 \rightarrow 14	Docetaxel		rare	13 \rightarrow 15/ 16	Taxol		yes
	GMPCPP				GMPCPP		
	Docetaxel				Alexa ₄₈₈ -Epo		
15/ 16 \rightarrow 15/ 16	Discodermolide		rare	15/ 16 \rightarrow 13	Fchitax-3		yes
	Fchitax-3				Docetaxel		

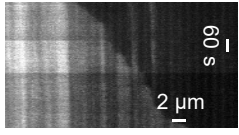
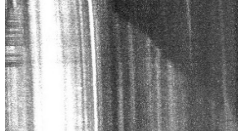
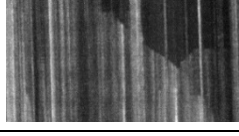

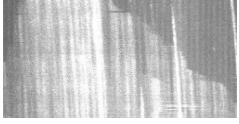
b



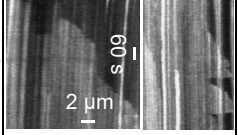
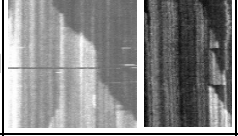
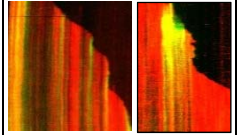
Supplementary Figure 4

bioRxiv preprint doi: <https://doi.org/10.1101/2021.02.11.430743>; this version posted February 11, 2021. The copyright holder for this preprint (which was not certified by peer review) is the author/funder, who has granted bioRxiv a license to display the preprint in perpetuity. It is made available under a [CC-BY-NC-ND 4.0 International license](https://creativecommons.org/licenses/by-nc-nd/4.0/).

Matching conditions

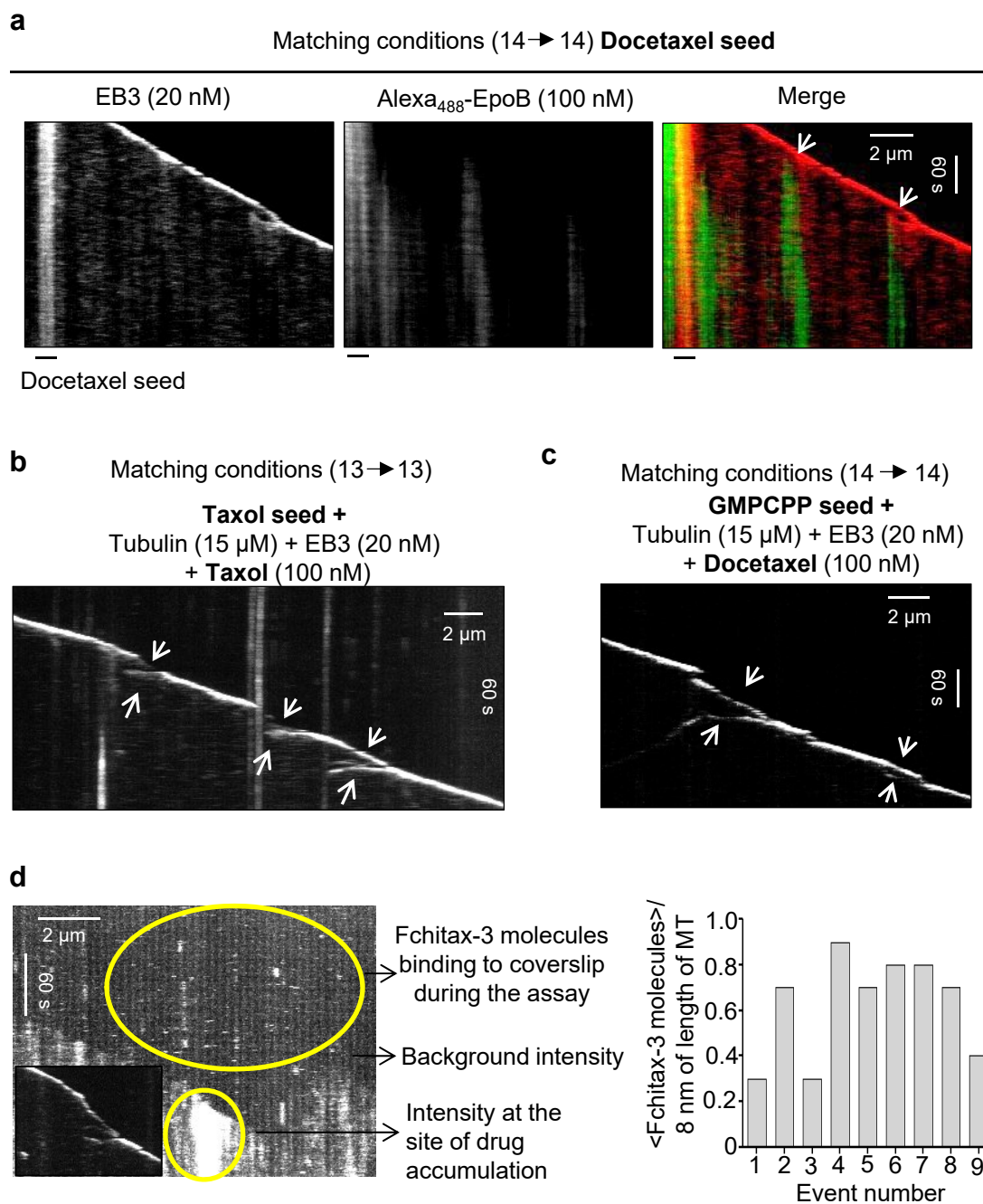
Tubulin (15 μ M) + MSA			
pf number	MT seed	MSA in the assay (100 nM)	Long depolym. events
13 \rightarrow 13	Taxol	Taxol 	rare
14 \rightarrow 14	GMPCPP	Docetaxel 	rare
	Docetaxel	Docetaxel 	
15/ 16 \rightarrow 15/ 16	Fchitax-3	Fchitax-3 	rare
	Fchitax-3	Discodermolide 	

Mismatching conditions

Tubulin (15 μ M) + MSA			
pf number	MT seed	MSA in the assay (100 nM)	Long depolym. events
14 \rightarrow 13	GMPCPP	Taxol 	yes
	Docetaxel	Taxol 	
14 \rightarrow 15/ 16	GMPCPP	Fchitax-3 	yes

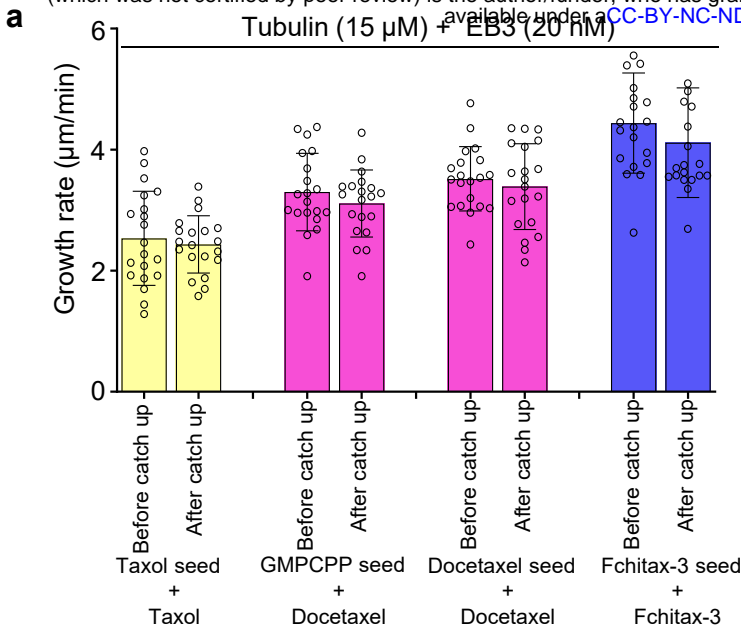
Supplementary Figure 5

<https://doi.org/10.1101/2021.02.11.430743>; this version posted February 11, 2021. The copyright holder for this preprint (which was not certified by peer review) is the author/funder, who has granted bioRxiv a license to display the preprint in perpetuity. It is made available under a [CC-BY-NC-ND 4.0 International license](https://creativecommons.org/licenses/by-nc-nd/4.0/).



Supplementary Figure 6

bioRxiv preprint doi: <https://doi.org/10.1101/2021.02.11.430743>; this version posted February 11, 2021. The copyright holder for this preprint (which was not certified by peer review) is the author/funder, who has granted bioRxiv a license to display the preprint in perpetuity. It is made available under a [CC-BY-NC-ND 4.0 International license](https://creativecommons.org/licenses/by-nc-nd/4.0/).



b

Intact MT				MT with a defect			
Thinner side diameter (Mean \pm sd, nm)	Thicker side diameter (Mean \pm sd, nm)	Mean diameter difference (nm)	N:diff < 2 nm Y:diff > 2 nm	Thinner side diameter (mean \pm sd, nm)	Thicker side diameter (Mean \pm sd, nm)	Mean diameter difference (nm)	N:diff < 2 nm Y:diff > 2 nm
27.0 \pm 0.3	27.5 \pm 0.2	0.5	N	25.6 \pm 0.5	26.6 \pm 0.3	1.0	N
26.3 \pm 0.6	26.9 \pm 0.4	0.6	N	27.5 \pm 0.2	28.1 \pm 0.2	0.6	N
26.7 \pm 1.1	27.3 \pm 0.3	0.6	N	27.9 \pm 0.3	30.4 \pm 1.3	2.5	Y
25.5 \pm 0.8	26.4 \pm 0.7	0.9	N	26.8 \pm 0.4	29.9 \pm 0.3	3.1	Y
26.3 \pm 0.7	26.6 \pm 0.8	0.3	N	20.9 \pm 0.4	26.7 \pm 0.1	5.8	Y
26.9 \pm 0.5	27.3 \pm 0.2	0.4	N	27.8 \pm 0.5	28.0 \pm 0.2	0.2	N
26.9 \pm 0.6	27.0 \pm 0.7	0.1	N	26.4 \pm 0.3	27.9 \pm 0.3	1.5	N
25.9 \pm 1.0	26.0 \pm 0.8	0.1	N	26.1 \pm 0.9	29.5 \pm 0.7	3.4	Y
26.6 \pm 0.7	26.9 \pm 0.6	0.3	N	25.3 \pm 0.7	26.4 \pm 0.8	1.1	N
27.1 \pm 0.5	27.1 \pm 0.7	0.0	N	27.2 \pm 0.2	28.7 \pm 0.4	1.5	N
27.1 \pm 0.5	27.1 \pm 1.2	0.0	N	24.3 \pm 0.4	25.8 \pm 0.9	1.5	N
26.6 \pm 0.3	27.3 \pm 0.8	0.7	N	24.2 \pm 0.1	26.2 \pm 0.5	2.0	Y
27.2 \pm 0.4	27.3 \pm 0.2	0.1	N	22.8 \pm 0.3	26.3 \pm 1.0	3.5	Y
27.6 \pm 0.3	27.6 \pm 0.8	0.0	N	25.0 \pm 0.3	28.6 \pm 0.6	3.6	Y
26.9 \pm 0.3	26.9 \pm 0.5	0.0	N	26.1 \pm 0.4	32.5 \pm 0.6	6.4	Y
27.7 \pm 1.0	27.8 \pm 0.2	0.1	N	26.5 \pm 0.2	27.0 \pm 0.4	0.5	N
28.1 \pm 0.2	28.8 \pm 0.3	0.7	N	27.1 \pm 0.5	30.1 \pm 0.8	3.0	Y
26.3 \pm 0.4	27.3 \pm 0.2	1.0	N				
27.0 \pm 0.7	29.5 \pm 0.7	2.5	Y				